THESIS FOR THE DEGREE OF DOCTOR OF PHILOSOPHY IN TERMO- AND FLUID DYNAMICS

Unsteady Numerical Simulations and Reduced-Order Modelling of Flows around Vehicles

JAN ÖSTH

Department of Applied Mechanics
Division of Fluid Dynamics
CHALMERS UNIVERSITY OF TECHNOLOGY
Göteborg, Sweden 2014

Unsteady Numerical Simulations and Reduced-Order Modelling of Flows around Vehicles
JAN ÖSTH
ISBN 978-91-7597-049-3

Doktorsavhandlingar vid Chalmers tekniska högskola
Ny serie nr. 3730
ISSN 0346-718X
Department of Applied Mechanics
Division of Fluid Dynamics
Chalmers University of Technology
SE-412 96 Göteborg
Sweden
Telephone: +46 (0)31-772 1000

Chalmers Reproservice
Göteborg, Sweden 2014

Unsteady Numerical Simulations and Reduced-Order Modelling of Flows around Vehicles
Thesis for the degree of Doctor of Philosophy in Termo- and fluid dynamics
JAN ÖSTH
Department of Applied Mechanics
Division of Fluid Dynamics
Chalmers University of Technology

Abstract

In this thesis several simulations have been carried out aimed at improving the knowledge of vehicle aerodynamics and improving the flow around vehicles with respect to the aerodynamic drag. Five flows around different simplified vehicle models have been considered in five appended publications. One tractor-trailer model, two passenger car models, one freight wagon model and one regional train model. In the simulations of the flow around the tractor-trailer model, the focus is on the flow in the gap between the tractor and the trailer and how this flow affects the global drag of the model. Large Eddy Simulation is used to simulate the flow around four variants of the model with different geometrical configurations. The behavior of the drag coefficient of the tractor-trailer model when varying the gap width and the shape of the front edges on the tractor is explained by identifying and analysing the large vortices around and in the the gap. The focus in the study on one of the passenger vehicle models is on the so-called A-pillar vortex. This is a swirling longitudinal vortex formed along the side windows on passenger vehicles due to the separation of the flow from the side edges of the front window and the engine hood. Flow control, both steady blowing and suction, from actuators located on the side of the front of the model, is applied in the LES simulations. Steady blowing into the vortex causes expedited breakdown of the vortex, which in turn influence the pressure distribution on the side windows and the overall drag of the model. Steady suction prevents the formation of the vortex, thereby removing the vortex entirely. Simulations aimed at improving the knowledge of the flow around a generic freight wagon model using LES is also reported. The model is smoothed in comparison to a real container wagon, but the overall geometrical features such as wheels and underhood are included. The simulations of the flow around the regional train model is done using Partially Averaged Navier Stokes (PANS). PANS is a recently proposed hybrid turbulence model for engineering types of flow. The regional train model consists of a bluff body with a length to height/width ration of 7:1. The flow around this model poses several challenging flow situations to simulate such as separation from the leading curved front edges, an attached boundary layer flow and separation from the curved rear edges at the moderate Reynolds number of 400 000 based on the models' width. An open cavity is placed on the model at the base and the drag is thereby decreased by some 10%. The second passenger vehicle model that has been investigated is a square back Ahmed body. This flow is simulated using LES, and the temporally and spatially resolved flow field is used as input to a Reduced-Order Model (ROM). The ROM is constructed by a decomposition of the flow field into spatially stationary modes with corresponding time-varying amplitudes, using the Proper Orthogonal Decomposition (POD). The introduction of the POD into the governing equations reduces these equations to a linear-quadratic dynamical system

with known coefficient. This system is then truncated, so that the remaining system contains a low number of modes. It is investigated how to best model the influence of the truncated high-frequency modes on the remaining system.

Keywords: Vehicle Aerodynamics, Numerical Simulations, Large Eddy Simulation, Reduced-Order Modelling

Preface

The work presented in this thesis was carried out at Chalmers University of Technology, at the Division of Fluid Dynamics in the Department of Applied Mechanics, under the supervision of Prof. Siniša Krajnović. The research was funded by the Swedish Traffic Administration. The simulations were carried out with resources provided by the Swedish National Infrastructure for Computing (SNIC) at C3SE, PDC and NSC.

Acknowledgements

I would firstly like to express my deep gratitude to my supervisor Prof. Siniša Krajnović for giving me this opportunity to broaden my knowledge in the very interesting field of CFD and vehicle aerodynamics, for giving me great support during the project, providing a very stimulating research atmosphere with state-of-the-art resources and also for being a very good academic role model, keeping a balance between focus on work and family.

I would like also like to express my sincere gratitude to Prof. Bernd Noack at Institute PPRIME at the University of Poitiers, France, for inviting me to a 3 months long research visit during the summer of 2013. Prof. Noack introduced me to the field of Reduced-Order Modelling, and the time, enthusiasm and effort he has spent on our joint research is beyond any resonable expectation. I would also like to thank PhD student Diogo Barros and his supervisor Prof. Jacquees Borée, also at the University of Poitiers, for sharing their experimental results and the stimulating joint research we have carried out on flow control. Many warm thanks goes also to PhD student Eurika Kaiser at the Institute PPRIME for the generosity of including me in her work on Cluster-based reduced order modelling. I also thank Prof. Laurent Cordier for taking his time to give private lectures on the theory of POD during my time in Poiters.

I would also like to thank all my collegues at the division of Fluid Dynamics for creating a great working environment. The ski trip to Hemsedal, Norway, in March 2014 studiously organized by Oscar Thulin is a memorable highlight. Special thanks to my roommate Eysteinn who's constantly making sure my Linux installation is top notch and helping me with other computer related issues. I would like to thank Dr. Yutaka Samuka at Railway Technical Research Institute (RTRI) for sharing results and details of his experimental work. The lecture series in fundamental fluid dynamics given by the now retired Ass. Prof. Gunnar Johansson at the division during the winter and spring of 2011/2012 is greatly appreciated. The lectures gave a possibility for reflection by going back to the fundamentals which was very stimulating.

The PhD project is sponsored by the Swedish Traffic Administration, without the funding and the involvement of Peter Larsson this project would not be possible. Software licenses were provided by AVL List GMBH for which we are very grateful. Special thanks goes also to Dr. Branislav Basara, Mr. Jürgen Schneider, Mr. Albert Van Der Meer and Dr. Wolfgang Schwarz at AVL for helping out with various issues regarding the software. Computations were performed at SNIC (Swedish National Infrastructure for Computing) at the Center for Scientific Computing at Chalmers (C3SE), Center for High Performance Computing at KTH (PDC) and National Supercomputer Center (NSC) at LiU. Least but not last I would like to thank my family for the support and encouragement and my girlfriend Sigfrið Guðmundsdottír who has brought unprecedented joy to my life.

List of Appended Publications

This thesis consists of an extended summary and the following appended papers:

Paper A J. Östh and S. Krajnović. "The flow around a simplified tractor-trailer model studied by Large Eddy Simulation." *J. Wind. Eng. Ind. Aerod.* **102** (2012), 36–47

Paper B S. Krajnović, J. Östh and B. Basara. "LES study of beakdown control of A-pillar vortex." *Int. J. Flow Control* **4** (2010), 237-257

Paper C J. Östh and S. Krajnović. "Simulations of flow around a simplified train model with a drag reducing device using Partially Averaged Navier- Stokes. *Conference on Modelling Fluid Flow (CMFF'12), The 15th International Conference on Fluid Flow Technologies.* Budapest, Hungary, 4-7 September, 2012

Paper D J. Östh and S. Krajnović. "A study of the aerodynamics of a generic container freight wagon using Large-Eddy Simulation." *J. Fluid. Struct.* **44** (2014), 31–51

Paper E J. Östh, B.R. Noack, S. Krajnović, D. Barros and J. Borée. On the need for a nonlinear subscale turbulence term in POD models as exemplified for a high Reynolds number flow over an Ahmed body. *J. Fluid Mech.* **747** (2014), 518–544

Division of work

Paper A The idea of the paper was developed by Jan Östh and Siniša Krajnović. The simulations and the analysis were carried out by Jan Östh. The manuscript was written by Jan Östh, with help from Siniša Krajnović.

Paper B The idea of the paper was developed by Siniša Krajnović and Jan Östh. The simulations were carried out by Jan Östh. The analysis was made by Siniša Krajnović and Jan Östh. The manuscript was written by Siniša Krajnović. Branislav Basara provided technical help with the simulation software that was used in the simulations.

Paper C The idea of the paper was developed by Jan Östh and Siniša Krajnović. The simulations and the analysis were carried out by Jan Östh. The manuscript was written by Jan Östh, with help from Siniša Krajnović.

Paper D The idea of the paper was developed by Jan Östh and Siniša Krajnović. The simulations and the analysis were carried out by Jan Östh. The manuscript was written by Jan Östh, with help from Siniša Krajnović.

Paper E The idea of the paper was developed by Bernd Noack, Jan Östh and Siniša Krajnović. The simulations and the analysis were carried out by Jan Östh. The manuscript was written by Jan Östh, with help from Bernd Noack and Siniša Krajnović. Diogo Barros and Jacquees Borée conducted the wind tunnel experiments that were used to validate the LES results with and also wrote Appendix A.

Other publications

Other publications related to the thesis by the author:

I S. Krajnović, J. Östh and B. Basara. "LES of active flow control around an Ahmed body with Active Flow Control". *Conference on Modelling Fluid Flow (CMFF'09), The 14th International Conference on Fluid Flow Technologies.* Budapest, Hungary, 9-12 September, 2009

II J. Östh and S. Krajnović. "A LES Study of a Simplified Tractor-Trailer Model". *The Aerodynamics of Heavy Vehicles III: Trucks, Buses, and Trains.* Vol. 1. Potsdam, Germany, 2010

III J. Östh and S. Krajnović. "Large Eddy Simulation of the Flow around one Single-Stacked Container Freight Wagon". *Proceedings of the First International Conference on Railway Technology: Research, Development and Maintenance.* Ed. by J. Pombo. Vol. 1145. Lecture Notes in Computer Science. Civil-Comp Press, Stirlingshire, Scotland, paper 162, 2012, pp. 51-66

IV J. Östh and S. Krajnović and D. Barros and L. Cordier and B.R. Noack and J. Borée and T. Ruiz. "Active flow control for drag reduction of vehicles using large eddy simulation, experimental investigations and reduced order modelling". *Proceedings of the 8th International Symposium On Turbulent and Shear Flow Phenomena (TSFP-8).* Poitiers, France, 2013

V E. Kaiser, B.R. Noack, L. Cordier, A. Spohn, M. Segond, M. Abel, G. Daviller, J. Östh , S. Krajnović and Niven, R. T. Cluster-based reduced-order modelling of a mixing layer. *Journal of Fluid Mechanics* (in print) 2014

Contents

Part I
Extended Summary

This thesis consists of an extended summary and five appended publications. Firstly, in chapter 1, the work in the appended publications is put into a general context of bluff body flows and vehicle aerodynamics. Then, in chapter 2. the general mathematical theory of fluid flows, and the specific numerical methods that have been used in this thesis are outlined. The concept of Reduced-Order Modelling (ROM) is then presented in chapter 3, followed by a summary of the appended papers in chapter 4. Additional results that are not already included in the appended papers are presented in chapter 5, and some concluding remarks are given in chapter 6. The extended summary is followed by the appended papers which are the major part of this thesis.

1 Introduction

This chapter begins by a brief introduction of flows around bluff bodies in section 1.1, as all flows around ground vehicles essentially are bluff body flows. This is followed by an introduction of specific issues concerning the flow around road vehicles in section 1.2, which is then followed by an outline of aerodynamic issues concerning railway systems in sections 1.3 and 1.4.

1.1 Bluff body flows

The term bluff body flows refer to flows over bodies which is strongly influenced by flow separation due to the geometrical shape of the body. The separation occurs either on the front or at the base of the body, or at multiple locations. The flow behind a bluff body is known as the 'wake'. The particularities of the flow around bluff bodies make the pressure drag on the body to dominate over the viscous drag on the body. The flow around bluff bodies is characterized by the Reynolds number of the large scales, defined as

$$Re_D = \frac{U_\infty D}{\nu}, \tag{1.1}$$

where U_∞ is the free-streaming velocity, D is a length scale characteristic of the size of the bluff body and ν is the kinematic viscosity of the fluid. Probably the most well-studied bluff body flow is the flow around an infinite long circular cylinder. This flow is characterised by the Reynolds number based on the diameter, D, of the cylinder. For small Reynolds numbers, $Re_D < 200$, the flow is laminar. However, the flow in the wake in this laminar regime undergoes three different states of organisation. For $Re_D < 5$ (see figure 1.1a), the flow stays attached on the cylinder everywhere on the body, and the flow can mathematically be described by potential theory. For $5 < Re_D < 30$ (see the top figure 1.1b), the flow separates at the base of the cylinder forming a steady near-wake.

This wake starts to oscillate in a periodic manner for $30 < Re_D < 200$ (see figure in the middle and bottom of 1.1b) [1].

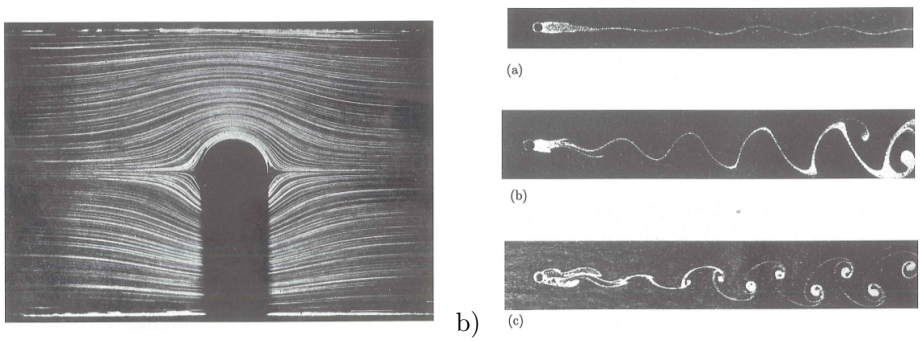

Figure 1.1: Flow regimes for the laminar cylinder wake. The pictures are taken from Zdravkovich [1].

The periodic shedding of vortices downstream of any body is referred to as the *von Kármán vortex street*, after the famous fluid dynamicist. The shedding occurs at a specific frequency, known as the natural frequency. For cylinders, the natural frequency is around 0.20, expressed in the non-dimensional Strouhal number, St, defined as

$$St = \frac{fD}{U_\infty}, \tag{1.2}$$

where f is the frequency in physical dimensions. The shedding is initiated by the interaction in the wake of the upper and lower shear layers separating from the cylinder. The two shear layers roll up in the wake and form a vortex that is convected downstream by the flow. As the Reynolds number increases, the interaction of the shear layers occurs closer to the base of the cylinder. For Reynolds numbers between $200 < Re_D < 10000$, the flow undergoes transition to the turbulent flow regime. This transition occurs firstly downstream in the wake. As the Reynolds number approaches $Re_D \sim 400$, the vortices themself start to become turbulent [2]. The shear layers separating from the lower and upper sides of the cylinder themselfs are laminar up to $Re_D = 30000$ [2]. This makes them separate on the front half of the cylinder. When the shear layers become turbulent, the separation point moves to the downstream half of the cylinder, and the pressure distribution along the cylinder surface is significantly altered due to this, resulting in the famous drag crisis where the drag of a cylinder drops by some 50% over a small range of Reynolds number.

For three-dimensional bluff bodies such as vehicle-like rectangular blocks as the one shown in figure 1.2a), the flow in the wake is more complicated. This is due to the presence of four boundary layers along the sides of the bluff body that separate into free shear layers in the wake. As the characteristic velocity in the shear layers, U_s, is of the same order as the free-streaming flow, U_0, but the velocity in the separated region in the wake, U_w, is less, there are four mixing layers forming in the wake. These mixing layers

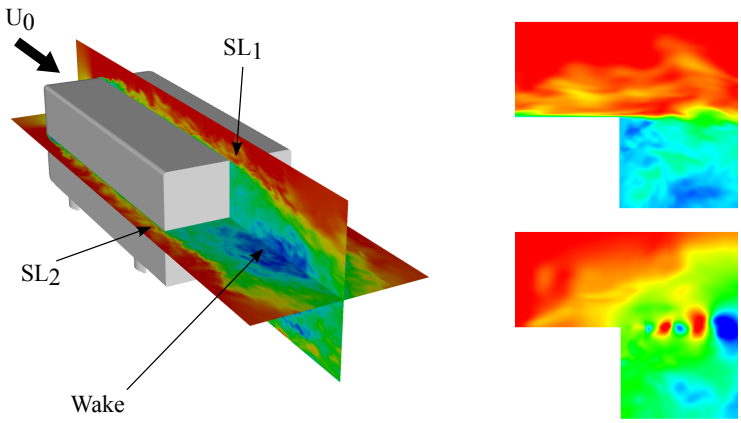

a) b)

Figure 1.2: Example of bluff body flow. a) flow over a rectangular bluff body; b) The shear layer SL_1 separating into a mixing layer. The top figure shows the streamwise velocity component, and the lower figure shows the pressure with signatures of the Kelvin-Helmholtz instability.

also start to interact with each other in a similar but more complex manner as the shear layers interact in the two-dimensional cylinder wake. Present in the mixing layers is also a fundamental unsteadiness known as the Kelvin-Helmoltz instability, or Kelvin-Helmoltz vortices [3]. These instabilities are born in the mixing layer between two flow regions at different velocities and produces turbulence kinetic energy. In figure 1.2a), two shear layers, SL_1 and SL_2, are pointed out for clarity. In figure 1.2b), the upper shear layer SL_1 is shown in a close-up view. The upper figure shows the streamwise velocity component, and the lower figure shows the pressure in the same instant. The pressure shows the signatures of the growing Kelvin-Helmholtz instability.

1.2 Road vehicle aerodynamics

Road vehicles, either passenger cars, trucks or buses, are heavily influenced by the sourrounding air during operations. Perhaps the most well-known issue is the influence of the air resistance (the *drag*) on the fuel consumption of the vehicle. However, there are also other concerns that must be taken into consideration when designing vehicles. Examples of such issues are the accumulation of dirt, water and snow on the wind shields, lights, side-mirrors and windows, the noise generated by the flow of air over pertubing details of the vehicles, road stability of the vehicle due to sudden gusts of side-winds and the cooling of the engine compartment and wheel brakes. As for the drag on vehicles, it is typically responsible for some $75-80\%$ of the overall fuel consumption for a medium-sized

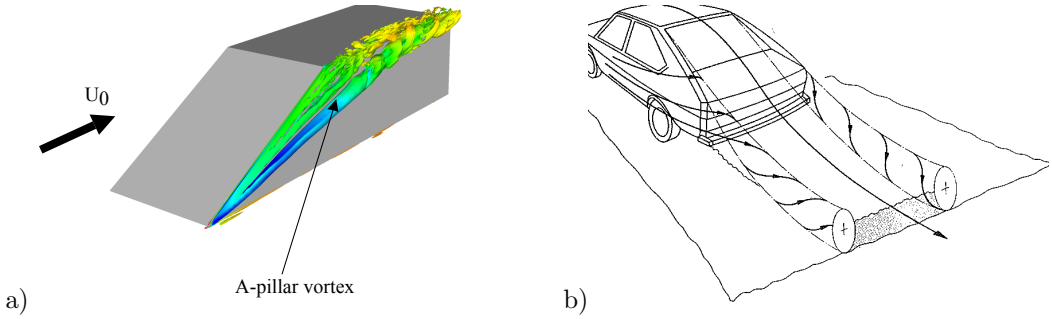

Figure 1.3: Examples of longitudinal vortices around passenger cars. a) A-pillar vortex; b) C-pillar vortex (picture taken from Hucho [4]).

passenger car when driving at 100 km/h [4].

Heavy duty vehicles, such as tractor-trailers, often has a more bluff geometrical shape, similar to the bluff body shown in figure 1.2. The European variant of heavy vehicles has a box-like front with curved front edges, which is followed by the trailer which most often is a of a rectangular shape with blunt edges. However, the tractor and the trailer are separated by a gap, which introduces additional complexity. Modern tractor-trailers typically have a sealed gap, in order to prevent the flow from impinging on the front of the trailer. Such an impingement increases the aerodynamic drag of the whole vehicle significantly. Moreover, the sealed gap prevents the separation on the leeward side of the tractor during side winds as well as the formation of recirculating flow in the gap. The flow in the gap, when not sealed, is dependent on the gap width between the tractor and the trailer. The structure of the flow in the gap and the connection between the flow structures and the aerodynamic drag are investigated in Paper A (*"The flow around a simplified tractor-trailer model studied by Large Eddy Simulation"*) in this thesis.

The streamlined shape of passenger cars introduces more complicated flow phenomena in addition to the four mixing layers discussed for a rectangular bluff body in the former section. Firstly, the presence of the ground can have an influence on the organisation of the flow in the wake and the pressure distribution on the base, especially on the lower part of the car. The streamlining of passenger vehicles also introduces the presence of trailing longitudinal vortex structures. These trailing vortices occur both on the front of the vehicle, where they are known as the A-pillar vortex (see figure 1.3a)), and on the rear part of fastback vehicles (sedan models) where they are known as C-pillar vortices (see figure 1.3b)). The breakdown of such longitudinal A-pillar vortices is investigated in the Paper B of this thesis (*"LES Study of breakdown control of A-pillar vortex"*).

These longitudinal vortices are rich in energy and are responsible for a large portion of the total aerodynamic drag (they are sometimes denoted "drag inducing vortices"). The level of vorticity in the separated shear layer that rolls in these longitudinal vortices is dependent on several geometrical conditions, of which the inclination of the edge at which

they separate from the body is most important. The stronger of the two pillar vortices is that around the C-pillar formed at the slanted back of a car, which has been studied extensively around the generic vehicle called the Ahmed body [7, 8, 9]. The formation of the longitudinal vortices around the C-pillar is similar to that around the A-pillar but there are also differences. The trailing vortices formed around A-pillars have an influence on both the aerodynamics and the aero-acoustics of passenger vehicles. According to a recent study by Alam et al. [10], the flow around the A-pillar is the main source of "in-cabin" aero-acoustic noise. The reason for the generation of aero- acoustic noise from the trailing vortex around the A-pillar can be found in fluctuating pressure on the surface of the car.

1.3 Railway aerodynamics

During the construction of railway systems, including the design of the actual train occupying the railway, there are several serious issues emerging concerning the flow of the air around the train and the influence of the flow induced by the train on the sourrounding environments that need to be taken into consideration. One issue is the fuel consumption affected by the aerodynamic drag, other issues are slipstreams, crosswind effects, pressure waves radiating from train tunnels entries, ballast projection and aeroacousticly generated sound.

Slipstreams are the air being dragged along by the train, i.e., the boundary layer forming on the sides of the trains. These boundary layers are very strong and can cause serious accidents on people and materials on station platforms when train passes without stopping. Accidents related to slip streams from 1972 to 2005 in the United Kingdom (UK) are summarized in [11]. The train industry is subjected to regulations concerning the allowed slipstream velocities around trains. In the context of the European railway network, this is regulated by the Technical Specification of Interoperability (TSI) of rolling stock, directive 2008/57/EG, which specifies that a train operating at 200 km/h at 1.2 m above the platform and a distance 3 m from the center of the track should not exceed 15.5 m/s. Slipstreams around high-speed trains have been investigated in experiments by Sterling et al. [12], by numerical methods by Muld [13], and around freight trains by Hemida et al. [14].

The wind velocity perpendicular to the motion of the train during traction is called the crosswind. At large crosswind speeds the side and lift forces cause a turning moment around the leeward rail that can, in extreme cases, cause overturning of the train and derailment. Several serious accidents where trains have been overturned by the crosswind have occured. Crosswinds and the influence of geometric design parameters on trains on the vortices formed on the leeward side causing low pressure have been investigated by unsteady numerical methods in Hemida [15] and Krajnović et al. [16].

When trains enter tunnels, the air inside the tunnel is compressed and a pressure wave forms that travels with the speed of sound through the tunnel. When the wave hits the exit of the tunnel, a part of the pressure wave is radiated to the surroundings and another

part is reflected. The part that is radiated to the surrounding environment cause noise pollution and the part that is reflected back into the tunnel eventually hits the train travelling inside the tunnel and causes considerable discomfort for the passengers inside the train by both induced noise and vibrations. Travelling inside tunnels also increases the drag of the train significantly [17, 18, 19] and causes increased mechanical stress on the train. Tunnels, although necessary to overcome superfluous ascents, cause restrictions on the railway operations. This is especially prevalent for single-track tunnels, where the ratio of the cross-sectional area of the train to the cross-sectional area of the tunnel is increased which leads to stronger pressure waves. Pressure waves and tunnel related aerodynamics are indeed a very important issue in the research on train aerodynamics [21, 20, 22]

Ballast projection is caused by the flow and pressure field underneath a train. The ballast consists of small gravel stones and rocks and as the train passes over them, the ballast stones can be dislodged and thrown against the undercarriage of the train. Flying stones phenomena underneath trains is referred to ballast flight. This can cause damage to the equipment underneath the train and the boogies. Underhood flow as been studied experimentally by, for instance, Jönsson et al. [23].

In addition to noise caused by mechanical interaction of parts on the train such as wheel/rail, aeroacoustic noise is produced by the train when driving due to the air flowing around the train. The source of the noise is flow separation caused by either the detachment of the boundary layer on the train or by vortex shedding from protruding structural elements on the train. The strengh of the noise is proportional to the speed of the train by a power of 6-8 [24]. Thus, the noise alleviation is of immense practical importance when train speed increases. Protruding objects on the train are the main source of aeroacoustic noise. For instance, the pantograph on the roof of the train which usually have a cylindrical shape can cause a monotone noise due to the vortex shedding behind it which propagates and pollutes the environment far away from the railway. All roughnesses on the train contributes to the aeroacoustic noise and also the nose shape of the train has a large impact. It is desirable to have a fore-body configuration with a long nose to reduce the aerodynamic noise [21].

1.4 Aerodynamic drag on trains

The sum of the resistive forces acting on trains in the direction of travel is usually expressed as a second order polynomial [25, 21, 27, 26]:

$$F = A + B \times V + C \times V^2 \tag{1.3}$$

It is assumed in (1.3) that the train does not accelerate or decelerate, that it travels on flat ground and that the railway is straight. Otherwise, terms for the forces needed to overcome the resistance of acceleration, the gravitational force and mechanical curving resistance must be included in (1.3). The term A on the right hand side contains mechanical resistances that are constant with respect to the speed of train, V, but whose magnitude is dependent on the number of axles, axle loads, track type and the length of

the train. The second term contains mechanical resistances coming from moving parts on the train and vary with the length of the train and are linearly proportional to the speed. The last term contains the aerodynamic resistance of the train, which is proportional to the square of the speed. The values of the coefficients in (1.3) are highly dependent on each specific type of train under consideration and must be determined individually for each specific train [28, 26, 27]. Empirical equations that can be used to estimate the resistance of a general train configuration have been developed. See [27] for a review of empirical equations used to estimate resistances of trains. A freight train normally consists of a large amount of wagons of different sizes, shapes and purposes. For a freight train, the coefficient C in (1.3) is the sum of the contribution to the aerodynamic drag from the locomotive and all wagons in the train. The size of the contribution to C of each wagon depends on the position of the wagon in the train [29] as well as on the spacing between the wagons [30, 31].

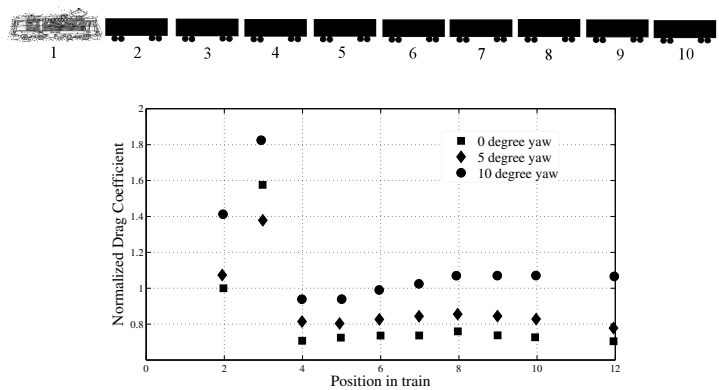

Figure 1.4: The top figure shows an arbitrary container freight train with a locomotive and 10 single stack wagons.The bottom figure shows the drag coefficient (y-axis) for a closed top gondola-type freight wagon depending on the position in the train (x-axis). All the values are normalized with the value of the drag coefficient of the wagon in the second position at zero yaw angle. The results are redrawn from the full-scale experimental study reported in [29].

Figure 1.4 shows the drag coefficient of a closed top gondola-type freight wagon depending on the position in the train. Results are shown for 0, 5 and 10 degrees of yaw angle. It is seen in the figure that, after the initial 3-4 wagons, the drag coefficient will reach some steady value that is some $20 - 50\%$ less than the drag coefficient of the second wagon. The majority of all the wagons in a freight train will experience an aerodynamic drag force slightly lower than that experienced by the first wagon in the train. The contribution to the total drag of the entire train from the locomotive will in turn be higher than the drag of the second wagon due to the stagnation pressure of the air on the front of the locomotive. A study reported in [32] suggests that the drag coefficient of the locomotive is in the order of 4 times of the drag coefficient of the first wagon (thus the

wagon in position 2 in figure 1.4). The total drag coefficient of a freight train consisting of a locomotive and 70 wagons of various sizes and shapes are estimated in [31] to be around 18.

Figure 1.5: Bombardier Contessa train used in Sweden for regional traffic.

A typical regional train consists of 3-4 units and its length is around 60-70 m. The operation of regional trains are characterized by short driving cycles ($\approx 1\,h$) where the trains make several stops during the cycle and the maximum speed is below $150 - 160$ km/h. Due to the stops, the part of the journey that the train has maximum speed is considerable shorter than the actual journey. This diminishes the relative influence of the aerodynamic drag on the total energy consumption.

One train used for regional traffic in Sweden is shown in figure 1.5. This is the Bombarbier Contessa train. As can be seen by a layman, the shape of the train is not optimal from an aerodynamic drag minimizing point of view. This is true in general for trains that are used for regional traffic. Less effort has been invested by the manufacturers on reducing the aerodynamic drag, due to it's relative less importance on the fuel consumption in comparison to high speed trains. The energy put into the railway system are consumed by different resistances. The energy demand for a general electric powered train is shown in figure 1.6.

The losses of the energy in the system are divided into the following components:

- E_{VI}: infrastructure losses
- E_{Vd}: driving losses
- E_{Vb}: braking losses
- E_{BR}: brake resistor losses

As is seen in figure 1.6, already some 20% of the energy provided by the substation is lost in the electric infrastructure on the way to the train. The driving losses E_{Vd}

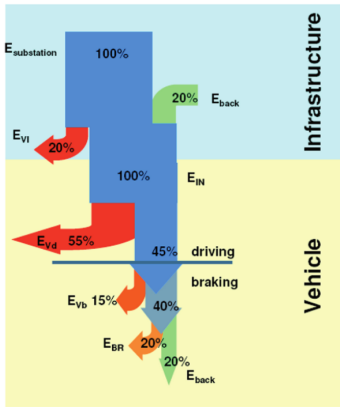

Figure 1.6: Traction energy demand distribution for railway system. The figure is taken from Orellano and Sperling [33]

corresponds to some 55% of the energy demand. This energy is dissipated to heat in the environment by the aerodynamic drag and mechanical resistances. This part cannot be regenerated, while some part of the energy that is converted to kinetic energy can be regenerated by the braking system.

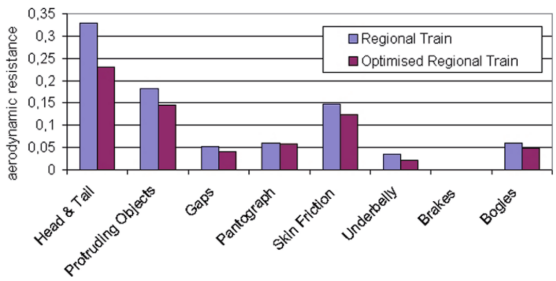

Figure 1.7: Estimated potential for reducing the drag of a regional train. The figure is taken from Orellano and Sperling [33]

The driving losses E_{Vd} are caused by the resistive forces acting on the train expressed in (1.3). In the estimate done in Orellano and Sperling [33] on a generic regional train on a typical driving cycle, a decrease in the aerodynamic drag coefficient of the train by 30% would lead to a 13 % decrease in the traction energy. There thus exists some potential for energy savings by improvement of the aerodynamics of regional trains. The total drag of a regional train comes from different parts on the train, as for freight trains. An estimate of the contribution to the drag and potential for reduction is shown in figure 1.7. The pressure drag from the head and the tail of the train accounts for some 30% of the

total. Other main sources are the various protroduing objects and the skin friction. The paper C (*"Simulations of flow around a simplified train model with a drag reducing device using Partially Averaged Navier-Stokes"*) and paper D (*"A study of the aerodynamics of a generic container freight wagon using Large-Eddy Simulation"*) of this thesis concerns the simulation of flow around a simplified regional train and a simplified freight wagon, respectively.

2 Numerical simulations of turbulent flows

This chapter starts with a general description of turbulent flows in section 2.1. Then, in section 2.2, the method of Large Eddy Simulation (LES) will be outlined. In section 2.3, the Partially Averaged Navier-Stokes method of turbulence simulation is described, and in section 2.4, the numerical details are provided in brief.

2.1 Turbulent flows and governing equations

Almost all flows encountered in engineering and daily life are turbulent. There exists no exact definition of what turbulence really is [36], but turbulent flows do have certain recognizable characteristics. They are, e.g., intrinsically complex, nonlinear and there is a large spread of the time and spatial scales in the flow [37]. The swirling motions observed in daily life such as flowing water in rivers, the pillars of air from plumes, the air around vehicles, are all examples of turbulent flows where the chaotic behavior of turbulence is visible to our eyes by the natural flow visualisation. Other characteristics of turbulent flows are irregularity and randomness. Turbulence is an omnipresent phenomenon whether it is in the processing of fluids and gases in pumps, compressors, pipes, the flow around vehicles such as airplanes, automobiles, trains, ships, or the mixing of air and fuel in engines and air and reactants in chemical reactors. Thus, there is no way to avoid the influence of turbulence nor to ignore it when constructing and studying such systems. The scientific study of turbulence takes different approaches, such as the statistical approach enabled by the Reynolds decomposition [38]. That is, to ignore the details of the instantaneous flow and instead regard the flow as a superposition of a statistically well-defined mean part and a fluctuating part. This allows for the use of statistical and probabilistic methods to study the nature of turbulence. Another approach is the phenomenlogical approach where the actual geometrical features of the instantaneous turbulence are characterized and universal coherent and incoherent structures are identified and interpreted. Such coherent features are, for instance, hairpin vortices in the turbulent boundary layer [39] and the near-wall streaks [40, 41].

It is generally accepted that the Navier-Stokes equations (NSE) mathematically model the turbulent flow of fluids at a macroscopic level and accurately describes what is observed in nature, even though no mathematically unique and smooth (continuously differentiable) solutions at high Reynolds numbers have been proven to exist so far [42]. NSE for an incompressible, single-phase flow, with dynamic viscocity μ and density ρ read:

$$\frac{\partial u_i}{\partial x_i} = 0. \tag{2.1}$$

$$\frac{\partial u_i}{\partial t} + u_j \frac{\partial u_i}{\partial x_j} = -\frac{1}{\rho}\frac{\partial p}{\partial x_i} + \nu \frac{\partial^2 u_i}{\partial x_j \partial x_j} + f_i. \tag{2.2}$$

Equation (2.1) is the continuity equation expressing the conservation of mass and (2.2) is the momentum equations expressing conservation of momentum. $u_{i=x,y,z} = u_i(x, y, z, t)$

are the three components in the velocity vector in a Cartesian coordinate system, $\nu = \mu/\rho$ is the kinematic viscocity of the fluid and f_i possible body forces, such as gravity.

In vehicle aerodynamics, the single most important parameter characterizing any flow around vehicles is the Reynolds number of the large scales. The Reynolds number is an appreciation of the ratio of the magnitude of the convective term (second term on l.h.s. in (2.2) to the magnitude of viscous term (second term on r.h.s. in (2.2)). The convective term is a nonlinear term which is the source of the irregularity, randomness and chaotic behavior of turbulent flows. Thus, the higher the Reynolds number is in a flow, the more pronounced is the influence of turbulence. For a sufficiently low Reynolds number, the flow is laminar. This is due to the viscous forces being large enough to be able to dampen out any non-regular fluctuation in the flow. When the Reynolds number increases, the relative ratio between the convective term and the viscous term increases, and the viscous term is not strong enough to be able to dampen out fluctuations, but they are instead magnified in a non-linear way by the convective term.

For passenger cars the Reynolds number, based on a representive length scale L, on roads during normal cruising speed is in the order of $10^6 - 10^7$ and for trains they are in the order of $10^7 - 10^8$. The scales in turbulent flows range from vortices and swirling motion of the size of L down to the smallest scales in the flow, the so called Kolmogorov scales, which are smaller than millimeters for vehicle flows. The large scales carry most of the kinetic energy of the fluid, while the dissipation of the kinetic energy of the fluid to internal energy (heat) takes place at the smallest scales. This is illustrated in figure 2.1, where l_0 is the characteristic size of the anisotropic energy-carrying scales, l_{EI} is a limit where the energy-carrying scales can be considered to be isotropic and, according to Kolmogorov theory, the statistics is universal [43, 44]. This range is called the *universal equilibrium range* and consists of two subranges, the *inertial subrange* and the *dissipation range*.

According to Kolmogorov's second similarity hypothesis the motion in the inertial subrange is determined primarily by inertial effects, thus viscous effects being negligible. The motion in the dissipation range is governed by strong viscous effects and are thus responsible for essentially all of the energy-dissipation [45]. The process in that kinetic energy is transferred from the large, energy-carrying scales through the inertial subrange to the dissipation scales is called the *Cascade-process*.

When numerically solving (2.1) and (2.2) all scales of motion need to be resolved in order to obtain an accurate representation of the real flow. That is, all the scales from the large scales down to the smallest, dissipative scales, must be resolved. This numerical approach is called Direct Numerical Simulation (DNS) [46]. DNS is used to study fundamental flows, such as isotropic turbulence [48, 47], turbulent boundary layers [49] and turbulent pipe flows [50]. Due to the very small character of the dissipative scales, the computational cost for such simulations is unfeasible for most engineering types of flows. Thus, a model is needed to get an approximation of the full DNS solution of the flow. By introducing the Reynolds decomposition that divides the flow into a superposition of a

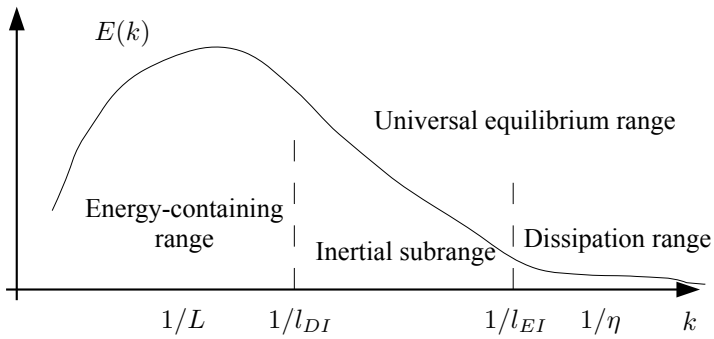

Figure 2.1: Idealized picture showing the energy content in a turbulent flow as a function of the wave number k (logaritmic scale).

mean part and a fluctuating part, in the following way

$$u_i = \langle U_i \rangle + u', \tag{2.3}$$

into the governing equations (2.1) and (2.2), the Reynolds Averaged Navier Stokes (RANS) equations are obtained. This approach is the basis for steady state engineering turbulence models such as the $k - \epsilon$ model and various Reynolds Stress Models. This method presupposes a large separation of the turbulent fluctuating scales and the energy-carrying scales (the "mean" flow). As this is not the case in most types of bluff body flows, but the scales are continously distributed from the large scales to the smallest, it is not correct to employ this type of methods to vehicle aerodynamics. In this thesis, the method of Large Eddy Simulation (LES) has been used as well a recently developed unsteady method called Partially Averaged Navier Stokes (PANS). Although both LES and PANS are unsteady, they are fundamentally different. In the coming sections, LES, being a rather well-known method, will only briefly be described, while a more elaborate outline of PANS is provided.

2.2 Large Eddy Simulation

Large Eddy Simulation (LES) is a collective term used to denote certain methods which are all based on the same conceptual idea that the large, energy-carrying scales are resolved directly while the small scales (the universal scales according to Kolmogorov theory) are not resolved, but the influence of them on the large scales is modelled. The physical motivation behind this idea is the assumption of the universality of the small scales described briefly in the former section. An implicit prerequisite for the idea of LES to work is that the large scales are resolved down to the inertial subrange where the scales presumably become isotropic. In practise, this is done by careful selection

of the applied numerical grid when carrying out the simulation of the flow. There are many ways in which LES can be done numerically, such as the spectral method which is based on the spectral NSE (the Fourier transformation of (2.2)), implicit LES where the numerical dissipation from the discretization schemes is used to balance the equations and thereby resolving only the large scales, and explicit sub-grid models where an explicit mathematical model is used to model the influence of the smallest scales on the resolved ones, after a spatial filter has been applied to the NSE. The latter method is the one used in this thesis. No comprehensive investigation or complete review of methods are provided herein, the reader is referred to e.g. Pope [36] and Sagaut [51] for a detailed theoretical analysis of LES, different sub-grid models and the mathematical foundations of the method. Herein the specific sub-grid model (the standard Smagorinsky Model [52]) that has been used in this thesis will be described. The governing equations of LES (the filtered Navier-Stokes) are obtained by applying a spatial filter on (2.1) and (2.2). The general filter operation applied on an arbitrary function $f = f(\boldsymbol{x}, t)$ (denoted by "overbar") is defined by:

$$\overline{f}(\boldsymbol{x}, t) = \iiint G(\boldsymbol{r}, \boldsymbol{x}) f(\boldsymbol{x} - \boldsymbol{r}, t) d\boldsymbol{r}. \tag{2.4}$$

The filter function, $G(\boldsymbol{r})$, must satisfy the normalization condition

$$\iiint G(\boldsymbol{r}, \boldsymbol{x}) d\boldsymbol{r} = 1. \tag{2.5}$$

The LES concept is based on the decomposition of the velocity field into the resolved motion (filtered velocities and pressure) and the small-scale motion that are filtered away *a priori* (sometimes denoted sub-grid scales or residual field), i.e.:

$$\boldsymbol{u}(\boldsymbol{x}, t) = \overline{\boldsymbol{u}}(\boldsymbol{x}, t) + \boldsymbol{u}''(\boldsymbol{x}, t). \tag{2.6}$$

This decomposition should not be confused with the Reynolds decomposition mentioned in the beginning of the chapter. The most important difference being that the filtered velocity field, $\overline{\boldsymbol{u}}(\boldsymbol{x}, t)$, is a random field like the unfiltered instantaneous velocity field, while the ensembled averaged velocity of the Reynolds decomposition is not [36]. The residual field, $\boldsymbol{u}''(\boldsymbol{x}, t)$, is never obtained explicitly in any LES simulation, and can only be obtained if a fully resolved DNS simulation has previously been conducted with exactly the same initial and boundary conditions and a finer grid. By applying the filter operation defined in (2.4) on the incompressible NSE, the filtered incompressible NSE are obtained:

$$\frac{\partial \overline{u}_i}{\partial x_i} = 0. \tag{2.7}$$

$$\frac{\partial \overline{u}_i}{\partial t} + \overline{u}_j \frac{\partial \overline{u}_i}{\partial x_j} = -\frac{1}{\rho} \frac{\partial \overline{p}}{\partial x_i} + \nu \frac{\partial^2 \overline{u}_i}{\partial x_j \partial x_j} - \frac{\tau_{ij}^R}{\partial x_j}, \tag{2.8}$$

where the force term has been dropped for convenience. The last term is the residual stress tensor, $\tau_{ij}^R = \overline{u_i u_j} - \overline{u}_i \overline{u}_j$. This part is split into an anisotropic part and an isotropic

part: $\tau_{ij}^R = \tilde{\tau}_{ij}^r + \frac{1}{3}\tau_{kk}^R\delta_{ij}$. The isotropic residual stress tensor is included in the filtered pressure, $\overline{p}$, and (2.8) is written as:

$$\frac{\partial \overline{u}_i}{\partial t} + \overline{u}_j\frac{\partial \overline{u}_i}{\partial x_j} = -\frac{1}{\rho}\frac{\partial \overline{p}}{\partial x_i} + \nu\frac{\partial^2 \overline{u}_i}{\partial x_j \partial x_j} - \frac{\tilde{\tau}_{ij}^r}{\partial x_j}, \tag{2.9}$$

In the standard Smagorinsky model, the anisotropic part of the residual stress tensor is modelled by an eddy-viscosity assumption:

$$\tau_{ij}^r = -2\nu_{sgs}\overline{S}_{ij}. \tag{2.10}$$

That is, the unresolved scales are said to be proportional to an artificial "eddy"-viscosity and the rate-of-strain tensor of the filtered velocities $\overline{S}_{ij} = \frac{1}{2}(\frac{\partial \overline{u}_i}{\partial x_j} + \frac{\partial \overline{u}_j}{\partial x_i})$. The eddy-viscosity, ν_{sgs}, is then modelled by a "mixing-length" hypothesis:

$$\nu_{sgs} = l^2\overline{S} = (C_s\Delta f)^2\overline{S}. \tag{2.11}$$

The eddy-viscosity is taken to be proportional to the square of a characteristic length scale of the unresolved scales and the magnitude of the rate-of-strain tensor. The length scale is taken to be the product of the filter width Δ and the Smagorinsky constant C_S. In this work, the filter width is taken to be the local grid size, $\Delta = (\Delta x \cdot \Delta y \cdot \Delta z)^{1/3}$ and the Smagorinsky constant is equal to $C_S = 0.1$, which is a value that has been used in numerous investigations of vehicle aerodynamics bluff body flows [54, 15, 53, 55]. It should be noted that, for complex geometries using non-equidistant computational grids as in the present thesis, a commutation error is introduced since the formulation of filtered equations ((2.7) and (2.8)) assumes that the filtering operation and spatial derivation commute. This is however not true on non-equidistant grids. The commutation error introduced is of the same order as the truncation error of a second-order linear interpolation scheme [56]. The function f in (2.11) is the Van Driest damping function

$$f = 1 - e^{-n^+/25}, \tag{2.12}$$

which is added to make ν_{sgs} vanish at the wall. n^+ is the wall-normal distance in viscous units. Although the Smagorinsky model is a rather simple sub-grid stress model, the method can be viewed from an mathematical point of view as adding a non-linear viscosity to the fluid since the filtering is never applied explicitly in the formulation of the method but it can just as well be implied implicitly. It turns out that the Smagorinsky model actually provides a regularization of the NSE that transforms the (possibly ill-posed) NSE into a well-posed set of partial differential equations, see e.g. Guermond et al. [57]. The LES method described in this section is used in paper A (*"The flow around a simplified tractor-trailer model studied by Large Eddy Simulation"*), paper B (*"LES Study of breakdown control of A-pillar vortex"*), paper D (*"A study of the aerodynamics of a generic container freight wagon using Large-Eddy Simulation"*) and paper E (*"On the need for a nonlinear subscale turbulence term in POD models as exemplified for a high Reynolds number flow over an Ahmed body"*) in this thesis.

2.3 Partially Averaged Navier-Stokes

In paper C (*"Simulations of flow around a simplified train model with a drag reducing device using Partially Averaged Navier-Stokes"*) in this thesis, the unsteady flow around a simplified train model is simulated using the recently developed unsteady method Partially Averaged Navier Stokes (PANS). The PANS method was proposed by Girimaji [59] as a bridging/hybrid approach of turbulence modelling for engineering types of flows developed from the first principles. The objective when deriving the method was to improve the inherent modelling defects of the Unsteady Reynolds Averaged Navier-Stokes approach (URANS). In an URANS simulation, the RANS equations are solved in a time-accurate fashion on a grid with a relatively good spatial resolution and with low turbulence kinetic energy and thus low eddy-viscosity on the inlet [60]. The intention with URANS is to resolve smaller unsteady scales of motion than those that are averaged away in steady RANS simulations. The URANS fails however, because the eddy-viscosity becomes to large and supresses the temporal and spatial fluctuations that could have been supported by the grid and temporal resolution. The failure of URANS is due to the ratio of produced turbulence kinetic energy to dissipation is too high (un-physical) which disables URANS to resolve the fluctuating motions [61]. PANS offers a method to prevent the eddy-viscosity to blow up by modifying the coefficients of the parent RANS model in a physical correct manner according to the local resolution of the flow field in time and space and the amount of resolved and unresolved fluctuations. The method thus seeks to maximize the amount of fluctuations that are resolved directly and which can be handled on a given grid and flow situation. To derive the PANS method, a model equation for the unresolved (sub-filter) kinetic energy, k_u, was derived from the equation of the generalized central moments [62]:

$$\begin{aligned}\frac{\partial \tau(u_i,u_j)}{\partial t}+\frac{\partial \tau(u_i,u_j)\bar{u}_k}{\partial x_k} &= -\frac{\partial}{\partial x_k}\{\tau(u_i,u_j,u_k)+\\ &\tau(p,u_i)\delta_{jk}+\tau(p,u_j)\delta_{ik}-\nu\frac{\tau(u_i,u_j)}{\partial x_k}\}\\ &+2\tau(p,S_{ij})-2\nu\tau(\frac{\partial u_i}{\partial x_k},\frac{\partial u_j}{\partial x_k}\\ &-\tau(u_i,u_k)\frac{\partial \bar{u}_j}{\partial x_k}-\tau(u_j,u_k)\frac{\partial \bar{u}_i}{\partial x_k}. \end{aligned} \tag{2.13}$$

Here, u_i are the instantaneous unfiltered / unaveraged instantaneous velocity variables and $\bar{u}_i = \langle u_i \rangle$ are the filtered /averaged velocities. The function $\tau(f,g) = \langle fg \rangle - \langle f \rangle \langle g \rangle$ is the generalized central moment of the functions f and g, and the angular brackets $\langle . \rangle$ correspond to a filter that is constant preserving and commutes with both spatial and temporal differentiation. In case of LES, this filter is the spatial filter defined in (2.4). Equation (2.13) is obtained by manipulation of NSE, in an analogous way to how the equations for the Reynolds stresses are obtained. The kinetic energy of the unresolved scales, k_u, is half of the trace of the central moment, $k_u = \frac{1}{2}\tau(u_k,u_k)$. An equation for the dissipation ϵ_u of the unresolved scales was constructed phenomenologically in the derivation of PANS. To

make PANS sensitive of the resolved scales of motion in the flow, the decisive parameters $f_k = k_u/k$ and $f_\epsilon = \epsilon_u/\epsilon$ (ratio of unresolved kinetic energy/dissipation to total kinetic energy/dissipation) were introduced into the derivation of the governing equations. How this was done will be explained in the coming paragraphs. It is important to stress that PANS is not a zonal LES/RANS model. It is a unique method based on derivations from the first principles, but having some features common with both RANS and LES inherent to it.

The original PANS [59] was derived using the standard $k-\epsilon$ RANS model as parent model. This model will be denoted PANS $k-\epsilon$ hereafter. The PANS $k-\epsilon$ method was tested on the flow around a square and circular cylinder by [63] and [64], respectively. As noted by Girimaji [59], the quality of the results in a simulation with PANS will be inherently dependent on the quality of the parent RANS model. Soon enough, a version of PANS based on the $k-\omega$ RANS model was introduced by Lakshmipathy and Girimaji [65]. In Girimaji et al. [61], the ratio of produced unresolved kinetic energy to dissipation in PANS was compared both theoretically and computationally with URANS and Detached Eddy Simulation (DES). It was found that PANS resolved more unsteady vortical structures than the two latter methods for the given cases and the employed grids, and PANS showed better agreement with experimental data. In Ma et al. [66] PANS was combined with a Low Reynolds Number (LRN) $k-\epsilon$ RANS model in order to correct the inherent inappropriate behavior of the PANS $k-\epsilon$ model near the wall due to the deficits in the standard RANS $k-\epsilon$ model. The performance of PANS LRN in standard cases such as decaying grid turbulence, turbulent channel flow and the periodic hill flow was investigated with promising results. It was also found that PANS LRN give better results than the Dynamical Smagorinsky LES model at a reduced CPU time for these cases.

Another method to enhance the performance of the k-ϵ RANS model in the near wall region is the four equation $k-\epsilon-\overline{v^2}-f$ RANS method proposed by Durbin [67] and later reformulated to the $k-\epsilon-\zeta-f$ model by Hanjalić et al. [68]. In these so called elliptic-relaxation based eddy-viscosity models, two additional (to k and ϵ) model equations for the the wall-normal velocity $\overline{v^2}$ scale and the relaxation function f, are derived and solved for. In the later formulation by Hanjalić et al. [68], the wall-normal velocity is normalized by the turbulence kinetic energy, such that $\zeta = \overline{v^2}/k$. The introduction of the wall-normal velocity $\overline{v^2}$ into the model enables RANS to take into account the inviscid wall blocking effect while incorporating low Reynolds number effects in the viscous and buffer sublayers of the turbulent boundary layer.

The PANS method based on RANS $k-\epsilon-\zeta-f$ was initially developed by Basara et al. [69] and further motivated in Basara et al. [70], where the model was validated against channel flow and the complex flow around a finite cylinder [71]. The PANS $\zeta-f$ version was used by Krajnović et al. [72] to simulate the complex and relatively high Reynolds number unsteady flow around the Rudimentary Landing Gear [73, 74] with promising results.

An overview of the derivation and the development leading up to the PANS model used in this thesis (PANS $\zeta-f$) follows here. The starting point is the partially filtered

Navier-Stokes equations:

$$\frac{\partial \bar{u}_i}{\partial t} + \bar{u}_j \frac{\partial \bar{u}_i}{\partial x_j} = -\frac{1}{\rho}\frac{\partial p_F}{\partial x_i} + \frac{\partial}{\partial x_j}(\nu \frac{\partial \bar{u}_i}{\partial x_j} - \tau(u_i, u_j)), \tag{2.14}$$

$$\bar{u}_i = \langle u_i \rangle; \quad p_F = \langle p \rangle. \tag{2.15}$$

$$\tau(u_i, u_j) - \frac{2}{3} k_u \delta_{ij} = -2\nu_u \bar{S}_{ij}. \tag{2.16}$$

Where u_i, p are the instantaneous unfiltered flow variables and $\bar{u}_i$, p_F are the partially averaged (filtered) flow variables. $\tau(u_i, u_j) = \langle u_i u_j \rangle - \langle u_i \rangle \langle u_j \rangle$ is the subfilter scale (SFS) stress which is closed by modelling its anisotropic part using the eddy-viscosity (Boussinesq) assumption (2.16). The partially averaged NSE are obtained by applying an implicit or explicit arbitrary filter on (2.1) and (2.2) that is constant preserving and commutes with both spatial and temporal differentiation, as is required by any filter to fulfill the averaging invariance [62]. The partial filtering is denoted by the angular brackets $\langle . \rangle$. In order to understand where the uniqueness of PANS lies, its must be noted that the filtered variables are of fundamentally different nature than the ensembled averaged variables in RANS, as well as the filtered variables in LES. The filtered PANS variables are stochastic variables as in LES, but the mean valued variables in RANS are not. However, the filtering in PANS is both spatial and temporal, and arbitrary, whereas in LES it is only spatial and definite. That is, the cut-off of the filtering in PANS is not defined a priori as in LES (in the inertial range), but is allowed to vary and is ultimately defined by the local velocity field in the simulation.

In (2.16), $k_u = \frac{1}{2}\tau(u_i, u_i)$ is the unresolved (subfilter) kinetic energy. The assumption in (2.16) is that the SFS-stress due to the unresolved scales are proportional to resolved rate-of-strain tensor, $\bar{S}_{ij} = \frac{1}{2}(\frac{\partial \bar{u}_i}{\partial x_j} + \frac{\partial \bar{u}_j}{\partial x_i})$ and by the eddy-viscosity of the unresolved motion ν_u. By choosing a spatial grid filter and letting $\nu_u = \nu_{sgs}$, the model described so far by (2.14), will be an LES approach. By letting the filtering be over all spatial and temporal scales of motion, the partially filtered velocities will in fact become the mean valued velocities (RANS), the SFS stresses will become the Reynolds stresses and ν_u will become the turbulent viscosity ν_T associated with RANS. If ν_u is set to zero then (2.14) will obviously yield a DNS solution if the employed grid is fine enough to permit resolving all the scales in the flow including the dissipative scales.

In the present work, the PANS methodology based on a four equations RANS model is used (PANS $\zeta - f$). This method was derived by Basara et al. [69], [70] in order to improve the inherent faulty modelling of the near wall physics by the parent RANS in the original PANS $k - \epsilon$ model. The four equation RANS model used is the elliptic-relaxation eddy-viscosity model $k - \epsilon - \zeta - f$ proposed in [68]. Thus, in the present work the eddy-viscosity of the unresolved motion is modelled as

$$\nu_u = C_\mu \zeta_u \frac{k_u^2}{\epsilon_u}, \tag{2.17}$$

where $\zeta_u = \overline{v_u^2}/k_u$ is the velocity scale ratio of the unresolved velocity scales $\overline{v_u^2}$ and k_u. $\overline{v_u^2}$ refers to the normal fluctuating component of the velocity field to any no-slip boundary. See Durbin [67] for further details and argumentation for the concept of introducing the normal velocity scale. In the RANS $k-\epsilon-\zeta-f$ model of [68], four model equations are solved in addition to the flow equations, one equation for each model variable respectively. The corresponding PANS model equations for the unresolved variables $k_u, \epsilon_u, \zeta_u, f_u$ take the form presented in the coming paragraphs. For details and a full motivation on all the steps on how the model equations are derived, follow the formal derivation of the PANS $k-\epsilon$ equations in [59] first and then the derivation of the PANS $\zeta-f$ equations in [69, 70].

$$\frac{\partial k_u}{\partial t} + \bar{u}_j \frac{\partial k_u}{\partial x_j} = (P_u - \epsilon_u) + \frac{\partial}{\partial x_j}[(\nu + \frac{\nu_u}{\sigma_{ku}})\frac{\partial k_u}{\partial x_j}]. \tag{2.18}$$

The equation above is the model transport equation for the unresolved kinetic energy. It is derived from the exact transport equation for the SFS stress, $\tau(u_i, u_j)$, (2.13). In (2.18), $P_u = -\tau(u_i, u_j)\frac{\partial \bar{u}_i}{\partial x_j}$ is the production of the unresolved kinetic energy. This term is closed by using the constituitive relationship in (2.16). The PANS model equation for the unresolved dissipation takes the form:

$$\frac{\partial \epsilon_u}{\partial t} + \bar{u}_j \frac{\partial \epsilon_u}{\partial x_j} = C_{\epsilon 1} P_u \frac{\epsilon_u}{k_u} - C^*_{\epsilon 2}\frac{\epsilon_u^2}{k_u} + \frac{\partial}{\partial x_j}(\frac{\nu_u}{\sigma_{\epsilon_u}}\frac{\partial \epsilon_u}{\partial x_j}). \tag{2.19}$$

$$C^*_{\epsilon 2} = C_{\epsilon 1} + \frac{f_k}{f_\epsilon}(C_{\epsilon 2} - C_{\epsilon 1}); \quad \sigma_{ku,\epsilon u} = \sigma_{k,\epsilon}\frac{f_k^2}{f_\epsilon}; \quad C_{\epsilon 1} = 1.4(1 + 0.045/\sqrt{\zeta_u}). \tag{2.20}$$

The PANS model equation for ϵ_u is developed from it's RANS counterpart [59]. Here, $\sigma_{k,\epsilon}$ are the turbulent transport Prandtl numbers known from RANS. $\sigma_{ku,\epsilon u}$ are the counterparts for the unresolved kinetic energy and dissipation, respectively. As was noted in [66], the parameters f_k and f_ϵ change the value of the turbulent transport Prandtl numbers and thus modifies the turbulent diffusion terms in the equations for k_u and ϵ_u. It was also found in [66] that this change of $\sigma_{ku,\epsilon u}$ by the unresolved-to-total kinetic energy and dissipation parameters contributes to the decrease of the unresolved eddy-viscosity ν_u. The PANS model equation for the unresolved velocity scale ratio ζ_u turns into:

$$\frac{\partial \zeta_u}{\partial t} + \bar{u}_j \frac{\partial \zeta_u}{\partial x_j} = f_u - \frac{\zeta_u}{k_u}P_u + \frac{\zeta_u}{k_u}\epsilon_u(1 - f_k) + \frac{\partial}{\partial x_j}(\frac{\nu_u}{\sigma_{\zeta u}}\frac{\partial \zeta_u}{\partial x_j}). \tag{2.21}$$

For the details on how the equation above was constructed, see [69, 70]. In doing so, it was however assumed that $f_\epsilon = \epsilon_u/\epsilon = 1$, i.e. that all the unresolved dissipation is in fact the RANS dissipation. This assumption is motivated by the assumption that the small dissipative scales are unlikely to be resolved, since that would require a spatial resolution of the computational grid beyond the inertial subrange, i.e. DNS like resolution. It was also noted in [75] that the range of the resolved scales decreased with decreasing f_ϵ. The variable f_u in (2.21) is the elliptic relaxation function for the unresolved velocity scales

ration ζ_u analogous to its RANS counterpart. The PANS Poisson equation for f_u is: [68, 69, 70].

$$L_u^2 \nabla^2 f_u - f_u = \frac{1}{T_u}(c_1 + c_2 \frac{P_u}{\epsilon_u})(\zeta_u - \frac{2}{3}). \tag{2.22}$$

The integral length and times scales L_u and T_u are computed using the unresolved kinetic energy. What is missing now is how the crucial parameter f_k is choosen. This will be explained in short. First, a summary of all the values for the constants in the equations is provided:

$$C_\mu = 0.22;\ C_{\epsilon 2} = 1.9;\ c_1 = 0.4;\ c_2 = 0.65;\ \sigma_k = 1;\ \sigma_\epsilon = 1.3;\ \sigma_{\zeta_u} = 1.2. \tag{2.23}$$

If the value of ratio of the unresolved to total kinetic energy is choosen to unity, i.e. $f_k = \frac{k_u}{k} = 1$, then the equations above collapse to the RANS equations. In the early work with PANS $k - \epsilon$ [59, 61, 63, 65], f_k was choosen as a fixed value constant in time and space during the entire simulation. As the influence of f_k on the resolved flow physics became clearer, a further step was taken in [76]. It was argued that the smallest value of f_k that a grid can support at any given location with instantaneous flow is given by:

$$f_k(\mathbf{x}, t) = \frac{1}{\sqrt{C_\mu}}(\frac{\Delta}{\Lambda})^{2/3}. \tag{2.24}$$

Where Δ is the geometric-average grid cell dimension, thus $\Delta = (\Delta x \cdot \Delta y \cdot \Delta z)^{1/3}$ and Λ is the Taylor scale of turbulence. In [77] f_k was implemented by the expression given in (2.24) as a dynamical parameter. The Taylor scale of turbulence Λ is computed using the resolved and unresolved kinetic energy and dissipation, $\Lambda = (k_u + k_{res})^{1.5}/\epsilon$. This is how it is done in the present work. f_k is computed at every location at the end of each timestep. The values are then used as fixed values during the next timestep. Thus, (2.14), (2.16), (2.17), (2.18), (2.19), (2.21), (2.22) and (2.24) make up the PANS $\zeta - f$ model used in the present work.

2.4 Numerical method

In this work numerical simulations of the flow around various ground vehicles have been performed and analysed. The branch of fluid dynamics dealing with the numerical methods of solving the governing flow equations is known as Computational Fluid Dynamics (CFD). In order to perform an simulation of the flow, the governing equations (in this thesis the incompressible NSE, (2.1) and (2.2)), must be discretized. There exists several methods to accomplish this, including: finite differences, spectral, finite elements and finite volumes being the most common. The discretization includes several steps where numerical schemes and interpolation methods must be choosen. In this work, the CFD simulations have been carried using the commercial finite-volume based CFD software AVL Fire [78]. Equations 2.1 and 2.2 are discretized by the solver using a collocated grid arrangement. The full details of the discretization and the solution algorithm are included in Appendix A.

For all simulations in this work, the time-marching is done using the implicit second-order accurate three-time level scheme:

$$\left(\frac{d\phi}{dt}\right)_n = \frac{3\phi^n - 4\phi^{n-1} + \phi^{n-2}}{2\Delta t_n} \ , \ \Delta t_n = t - t_{n-1} = t_{n-1} - t_{n-2}. \tag{2.25}$$

In the cases where LES simulations have been done, the convective terms in the momentum equations have been discretized using a blend between 95% central differences (CDS) and 5% upwinding of first order accurancy. The upwinding is needed to dampen numerical occillations caused by the CDS and local insufficient grid resolution. It's generally hard to accomplish 100% CDS for complex flow cases. In the case where PANS has been used, the convective terms have been discretized by using a second order upwinding scheme.

3 Reduced-Order Modelling (ROM

In the framework and context of the present work, the method of Reduced Order Models (ROM) is considered to simplify the NSE and reducing the computational effort of obtaining long-term flow solutions from solving numerically the full NSE to solving a set of coupled Ordinary Differential Equations (ODEs), while still maintaining important large-scale physical features in the flow. ROM can be used as a testbed for physical understanding of actual flow phenomena, as computationally inexpensive surrogate models for optimization and used as a low-order plant for control design.

The basis of a ROM is the separation of the temporal and spatial scales by a decomposition of the flow field into time-dependent amplitudes and spatially stationary modes. The modes being artificial velocity fields. In principle any set of functions forming a basis in the Hilbert space $L^2(\Omega)$ of square-integrable functions in the finite or periodic domain Ω can be used, such as Chebychev polynomials, Fourier modes or stability eigenmodes. This approach to ROM can be described as a mathematical or physical approach. Another approach is the empirical ROM, which relies on empirically computed modes from snapshots of numerically or experimentally obtained flow fields. A popular method used to compute modes is Proper Orthogonal Decomposition (POD) [38, 79], building on the Karhunen-Loève decomposition. Another approach is the recently developed method Dynamic Mode Decomposition (DMD) [80, 81] building on spectral analysis and the Koopman operator. These decompositions have different properties. The POD computes modes that are orthonormal and optimal in the sense that the modes in average maximize the kinetic energy contained in the modes compared to any other decomposition, (see , e.g., [82, 83, 79]), while the DMD trades the orthonormality and energy optimality in favor of information about the growth rate and frequency of the corresponding DMD modes. In the present work, the POD have been used as a basis of ROMs. The ROMs are built by using the empirical POD modes as a basis for a Galerkin system. The Galerkin system consists of a dynamical system of ODEs of the time-evolution of the modal amplitudes. These ODEs are obtained by the projection of the Navier-Stokes equation on the POD modes.

Reduced Order Models (ROMs) in the form of either empirical, mathematical or physical models have been studied for some, but by no means all, flow cases. Examples are the vortex shedding flow behind a circular cylinder at low Reynolds number [84, 85], the turbulent jet and mixing layer [87, 86, 88] and the lid-driven cavity flow [89]. The very first ROM was presented in the pioneering work of Aubry et al. [90], where a ROM was built in order to study the dynamical behavior of the coherent structures in the turbulent boundary layer. Aubry and co-workers used a mix of POD modes and Fourier modes and presented a low-dimensional model capable of capturing the major aspects of the ejection and bursting events that up to that date only had been observed in experimental work. They used a linear 'eddy-viscosity' model to include in their low-dimensional model the effect of the left-out higher order modes. Rempfer [91], [92, 93] studied the transitional flat-plate boundary layer and built a ROM for that flow. Rempfer used only

POD modes in his model. For the higher order modes that was left out in his ROM, he refined the linear model by Aubry et al. by using one eddy-viscosity for each of the higher order modes, i.e. 'modal eddy viscosities'. Galletti et al. [94] generalized the ansatz of modal eddy viscosities by adding an additional linear term to the Galerkin system. They demonstrated their model for the laminar flow around a confined square cylinder. The above closure models all assume a linear term for representing the nonlinear dynamics of the turbulence cascade governed by the convective term in the NSE. Using a linear model has been demonstrated to work well for low Reynolds number flows in the laminar and transitional regime. However, not many studies are reported with a successful outcome for broadband turbulence [95]. To overcome this deficiency, Noack et al. [95] proposed an ansatz that takes nonlinear effects into account based on the Finite-Time Thermodynamical (FTT) framework [96]. Nonlinear models based on Galerkin projection of filtered Navier-Stokes equations has also been pursued by [97, 98].

3.1 Galerkin Systems

In this section the derivation leading to an empirical Galerkin system is outlined. The modes in the system are taken to be the orthonormal modes obtained from a POD decomposition. A general velocity field $\boldsymbol{u} = (u, v, w)$ and the pressure field represented by p are considered in the steady finite domain, $\Omega \in \boldsymbol{R}^3$, with a Cartesian coordinate system $\boldsymbol{x} = (x, y, z)$ with unit vectors $\boldsymbol{e}_x, \boldsymbol{e}_y, \boldsymbol{e}_z$, respectively. The time is represented by t and the finite time intervall $[0, T]$ is considered. Firstly, in section 3.1.1, the POD is described and the method to compute the modes and the amplitudes of the decomposition. Secondly, in section 3.1.2, the Galerkin system is derived. In section 3.1.3, the Galerkin system is truncated to yield a reduced Galerkin system. Lastly, in section 3.1.4, closure methods for the reduced Galerkin system relevant to the thesis are outlined.

3.1.1 Proper Orthogonal Decomposition (POD)

The starting point is the NSE with corresponding initial and boundary conditions in the following form:

$$\partial_t \boldsymbol{u} + \boldsymbol{u} \cdot \boldsymbol{\nabla} \boldsymbol{u} + \frac{1}{\rho} \boldsymbol{\nabla} p - \nu \nabla^2 \boldsymbol{u} = \boldsymbol{R}(\boldsymbol{u}), \tag{3.1a}$$

$$\boldsymbol{\nabla} \cdot \boldsymbol{u} = 0, \tag{3.1b}$$

$$\boldsymbol{u}(\boldsymbol{x}, 0) = \boldsymbol{u}_{IC}(\boldsymbol{x}) \ \ \forall \boldsymbol{x} \in \Omega, \tag{3.1c}$$

$$\boldsymbol{u}(\boldsymbol{x}, t) = \boldsymbol{u}_{BC}(\boldsymbol{x}) \ \ \forall \boldsymbol{x} \in \partial\Omega, t \in [0, T]. \tag{3.1d}$$

Where $\boldsymbol{R}(\boldsymbol{u})$ is the residual of the momentum equation. Considering the fact that the pressure can be computed from the velocity field by the pressure-Poisson equation, the residual of the momentum equation can be considered to be a function of the velocity field, $\boldsymbol{u}$, only. The input to the POD is an ensemble of M time-discrete snapshots ($\mathbf{u}^m = \mathbf{u}(\mathbf{x}, t^m)$, $t^m = m\Delta t$, $m = 1, ..., M$) obtained from either experimental measurements or

numerical simulations. In this thesis, the snapshots are obtained from LES simulations. In POD [38], the velocity field, $\boldsymbol{u}(\boldsymbol{x},t)$, is firstly decomposed in a mean field, $\boldsymbol{u}_0$, and a fluctuating part, $\boldsymbol{u}'$, with zero mean, following the statistical approach of Reynolds (2.3). The fluctuating part is then decomposed by a separation of the spatial and temporal variables into a sum of products between an infinite number of space dependent modes $\boldsymbol{u}_i$, and the corresponding temporal evolution $a_i(t)$ of each mode:

$$\boldsymbol{u}(\boldsymbol{x},t) = \boldsymbol{u}_0 + \boldsymbol{u}' = \boldsymbol{u}_0 + \sum_{i=1}^{\infty} a_i(t)\boldsymbol{u}_i(\boldsymbol{x},t) \approx \boldsymbol{u}_0 + \sum_{i=1}^{N} a_i(t)\boldsymbol{u}_i(\boldsymbol{x},t). \tag{3.2}$$

In this work, the mean flow, $\boldsymbol{u}_0$, has been taken as the temporal average of the velocity over all of M snapshots, thus $\boldsymbol{u}_0 = \frac{1}{M}\sum_{m=1}^{M}\boldsymbol{u}^m$, and the fluctuations are computed by subtracting the mean flow from each snapshot, $\boldsymbol{u}_m^{'} = \boldsymbol{u}^m - \boldsymbol{u}_0$. In practise, a finite number of modes, N, are considered. The modes, $\boldsymbol{u}_i$, span a basis in the Hilbert space of square integrable vector fields $L^2(\Omega)$. The inner product between two vector fields $\boldsymbol{a}$ and $\boldsymbol{b}$ in the Hilbert space is given by the integral

$$(\boldsymbol{a},\boldsymbol{b})_\Omega = \int_\Omega \boldsymbol{a}\cdot\boldsymbol{b}\; d\boldsymbol{x}. \tag{3.3}$$

The modes are constructed in such a way that they are orthonormal, i.e.

$$\forall i,j \in \{1,...N\} \;\; : \;\; (\boldsymbol{u}_i,\boldsymbol{u}_j)_\Omega = \delta_{ij}, \tag{3.4}$$

where δ_{ij} is the Kronecker delta function. The vector norm in the Hilbert space is given by

$$||\boldsymbol{a}||_\Omega = \sqrt{(\boldsymbol{a},\boldsymbol{a})_\Omega}. \tag{3.5}$$

Using this norm, the turbulence kinetic energy in the domain, Ω, during each snapshot, $K^m(t) = K^m = K(t_m)$, can be expressed as

$$K^m = \frac{1}{2}||\boldsymbol{u}_m^{'}||_\Omega^2, \tag{3.6}$$

and the kinetic energy of the mean flow is given by

$$K_0 = \frac{1}{2}||\boldsymbol{u}_0||_\Omega^2. \tag{3.7}$$

More important properties of general interest and later reference are that each mode fullfills the continuity equation, i.e.

$$\boldsymbol{\nabla}\cdot\boldsymbol{u}_i = 0, \;\; i = 0,1,...N, \tag{3.8}$$

and that the boundary conditions are 'absorbed' by the mean flow [79, 95]

$$\forall \boldsymbol{x} \in \partial\Omega \;\; : \;\; \boldsymbol{u}_0(\boldsymbol{x}) = \boldsymbol{u}_{BC}(\boldsymbol{x}) \text{ and } \boldsymbol{u}_i(\boldsymbol{x}) = 0, \;\; i = 1,...,N. \tag{3.9}$$

The method of Snapshots [99, 79] is used in the present work to compute the empirical POD modes, $\boldsymbol{u}_i$ with corresponding amplitudes, $a_i(t)$. The Snapshot method produced

$N = M - 1$ modes. The method consists of 5 steps [95, 99]:

1. Compute the mean flow,

$$\boldsymbol{u}_0 = \frac{1}{M} \sum_{m=1}^{M} \boldsymbol{u}^m. \tag{3.10}$$

2. Compute the correlation matrix $C = (C^{mn})$ of the fluctuations,

$$C^{mn} = \frac{1}{M} (\boldsymbol{u}^m - \boldsymbol{u}_0, \boldsymbol{u}^n - \boldsymbol{u}_0)_\Omega. \tag{3.11}$$

3. Find the first N eigenvectors $\boldsymbol{v}_i = [v_1^i, ..., v_N^i]^T$ and the sorted eigenvalues $\lambda_1 \geq \lambda_2 \geq ... \geq \lambda_N \geq 0$ of the correlation matrix,

$$C\boldsymbol{v}_i = \lambda_i \boldsymbol{v}_i, \;\; i = 1, ..., N. \tag{3.12}$$

4. Compute each POD mode as a linear combination of the snapshot fluctuations and the eigenvalues,

$$\boldsymbol{u}_i = \frac{1}{\sqrt{N\lambda_i}} \sum_{m=1}^{M} v_m^i (\boldsymbol{u}^m - \boldsymbol{u}_0), \;\; i = 1, ..., M. \tag{3.13}$$

5. Compute the mode amplitudes,

$$a_i^m = \sqrt{\lambda_i N} v_m^i, \;\; i = 1, ..., N. \tag{3.14}$$

The computed amplitudes have a zero time-mean and are uncorrelated

$$\langle a_i(t) \rangle_T = 0, \;\; \langle a_i(t) a_j(t) \rangle_T = \lambda_i \delta_{ij}, \;\; i, j \in \{1, ..., N\}. \tag{3.15}$$

The turbulence kinetic energy in one fluctuation, K^m, (3.6), can be expressed as the sum of all modal contributions, $\boldsymbol{u}^{[i]} = a_i \boldsymbol{u}_i$:

$$K(t) = \sum_{i=1}^{\infty} K_i(t), \;\; \text{where} \;\; K_i(t) = \frac{1}{2} ||\boldsymbol{u}^{[i]}||_\Omega^2 = \frac{1}{2} a_i^2. \tag{3.16}$$

Thus, the total turbulence kinetic energy content as a function of time in each mode is given by $K_i(t) = \frac{1}{2} a_i^2$. The total kinetic energy in the system, $K^\infty(t)$, is given by

$$K^\infty(t) = K_0 + \sum_{i=1}^{N} K_i(t). \tag{3.17}$$

The POD method by definition returns modes that are ordered with respect to the turbulence kinetic energy in each mode, such that $K_1 \geq K_2 \geq ... \geq K_N$. Further on, time-averaged values are implicitly assumed when the dependence of t is dropped from a kinetic energy quantity, i.e., $K_i = \overline{K_i}(t)$.

3.1.2 Galerkin system

In this section the focus is on the derivation of evolution equations for the amplitudes, which will lead up to a dynamical system (Galerkin System) where the POD modes are used to compute the physical coefficients in the system. Compact notation is introduced here,

$$(F)_\Omega = \int_\Omega F \, d\boldsymbol{x}, \tag{3.18}$$

for the volume integral of F over the domain Ω, and

$$(F)_{\partial\Omega} = \oint_{\partial\Omega} F \cdot d\boldsymbol{A}, \tag{3.19}$$

for the surface integral of F over the boundary of the domain. The empirical orthonormal modes that were computed in the previous chapter form a set of orthonormal base functions in a Hilbert subspace. The first step that must be taken in order to construct the Galerkin System is to project the momentum and continuity equations (3.1) onto the subspace spanned by the modes. Before that is done, the decomposition is re-arranged in the following way

$$\boldsymbol{u}(\boldsymbol{x},t) = \boldsymbol{u}_0 + \sum_{i=1}^{N} a_i(t)\boldsymbol{u}_i(\boldsymbol{x},t) = \sum_{i=0}^{N} a_i(t)\boldsymbol{u}_i(\boldsymbol{x},t), \tag{3.20}$$

where $a_0 \equiv 1$, following the convention of Rempfer [91], Rempfer and Fasel [92], and Rempfer and Fasel [93]. The velocity $\boldsymbol{u}$ is now expanded in the residual of the momentum equation and projected on the POD modes

$$\left(\boldsymbol{u}_i, \boldsymbol{R}\left(\sum_{i=0}^{N} a_i(t)\boldsymbol{u}_i(\boldsymbol{x},t) \right) \right)_\Omega , \; i = 1, ..., N. \tag{3.21}$$

This step is known as the *Galerkin projection*. The Galerkin projection leads to four terms which are handled separatly for clarity. The projection of the time-derivative of the velocity leads to

$$\left(\boldsymbol{u}_i, \partial_t \left[\sum_{j=0}^{N} a_j(t)\boldsymbol{u}_j(\boldsymbol{x},t) \right] \right)_\Omega = \sum_{j=1}^{N} \dot{a}_j(t)(\boldsymbol{u}_i, \boldsymbol{u}_j)_\Omega = \dot{a}_i, \tag{3.22}$$

due to the steadiness of a_0 and the orthonormality of the modes. The projection of the viscous term reads

$$\left(\boldsymbol{u}_i, \nu\nabla^2 \sum_{j=0}^{N} a_j(t)\boldsymbol{u}_j(\boldsymbol{x},t) \right)_\Omega = \nu \sum_{j=0}^{N} l_{ij}^{\nu} a_j, \tag{3.23a}$$

$$l_{ij}^{\nu} = (\boldsymbol{u}_i, \nu\nabla^2\boldsymbol{u}_j)_\Omega = [\boldsymbol{u}_i \cdot \boldsymbol{\nabla}\boldsymbol{u}_j]_{\partial\Omega} - (\boldsymbol{\nabla}\boldsymbol{u}_i : \boldsymbol{\nabla}\boldsymbol{u}_j)_\Omega. \tag{3.23b}$$

The viscous term is transformed from containing the Laplacian to only first order derivatives by help of the Gauss theorem. This procedure is done in order to enhance the numerical accurancy when computing the terms.

The Galerkin projection of the convective term leads to

$$\left(\boldsymbol{u}_i, -\boldsymbol{\nabla}\cdot\left(\left[\sum_{j=0}^{N} a_j(t)\boldsymbol{u}_j\right]\left[\sum_{k=0}^{N} a_k(t)\boldsymbol{u}_k\right]\right)\right)_{\Omega} = \sum_{j,k=0}^{N} q^c_{ijk} a_j a_k \tag{3.24a}$$

$$q^c_{ijk} = -(\boldsymbol{u}_i, \boldsymbol{\nabla}\cdot(\boldsymbol{u}_j\boldsymbol{u}_k))_{\Omega}. \tag{3.24b}$$

The fourth and last term is the pressure term:

$$\left(\boldsymbol{u}_i, \frac{1}{\rho}\boldsymbol{\nabla} p\right)_{\Omega}. \tag{3.25}$$

As in the works of [84] and [100], the Galerkin projection of the pressure term was found to be negligible and is thus omitted from the model in the present study. We can now write the Galerkin system describing the temporal evolution of the modal coefficients, $a_i(t)$,

$$\dot{a}_i = \sum_{j=0}^{N} l^{\nu}_{ij} a_j + \sum_{j,k=0}^{N} q^c_{ijk} a_j a_k. \tag{3.26}$$

The coefficients l^{ν}_{ij} and q^c_{ijk} are called the *Galerkin coefficients* and are computed using the POD modes. The diagonal terms of the viscous coefficients, l^{ν}_{ii}, describe the viscous dissipation of turbulence kinetic energy to heat due to mode $\boldsymbol{u}_i$, and the off-diagonal elements, l^{ν}_{ij}, is the viscous dissipation due to the interaction of mode $\boldsymbol{u}_i$ and mode $\boldsymbol{u}_j$. The quadratic convective term, q^c_{ijk}, describe the triadic interactions between the modes, i.e., turbulence energy transfer between mode $\boldsymbol{u}_i$ and the modes $\boldsymbol{u}_j$ and $\boldsymbol{u}_k$. Thus, the Galerkin coefficients contain highly desirable information about the physical behavior of a considered flow system.

3.1.3 Reduced Galerkin system

The dynamical system in (3.26) is a closed system of Ordinary Differential Equations (ODEs) with known coefficients. By integrating this system in time further long-term information about the dynamical behavior of the system can be obtained. However, the aim is to simulate the dynamical behavior of the "large" scales, that presumably govern the global physics around a bluff body. This is desirable since the computational time of computing the convective term, q^c_{ijk}, and integration the system in time scales as $\sim N^3$, so that the computational effort soon exceeds the computational effort of the original LES simulation. It is desired to build a ROM that contains the important physics, but with a computational effort to build and to integrate in time that is much less than the time of solving the original LES simulations. We therefore choose a reduced number of modes K,

that will form our ROM such that $K < N$. The corresponding dynamical system takes the following form:

$$\dot{a}_i = \sum_{j=0}^{K} l_{ij}^{\nu} a_j + \sum_{j,k=0}^{K} q_{ijk}^{c} a_j a_k + g_i(\boldsymbol{a}), \ , \ i = 1, ..., K. \tag{3.27}$$

The residual $g_i(\boldsymbol{a})$ is the sum of the viscous and convective terms of all modes of higher number than K:

$$g_i(\boldsymbol{a}) = \sum_{j=K+1}^{N} l_{ij}^{\nu} a_j + \sum_{\substack{j,k=0 \\ max\{j,k\}>N}}^{N} q_{ijk}^{c} a_j a_k \tag{3.28}$$

In the Kolmogorov description of the turbulence Cascade [45, 43, 36], the large, energy-carrying scales transfer energy to successively smaller scales, and most of the dissipation of the turbulence kinetic energy to internal energy (heat, vibrational energy, etc) of the molecules takes place at the smallest relevant scales, the Kolmogorov scales. Therefore, any attempt to solve the reduced system in (3.27) leaving the residual, $g_i(\boldsymbol{a})$, out, will lead to blow up of energy in the resolved modes and divergence of the system. Thus, the influence of the left out higher order modes needs to be modelled

3.1.4 Closure methods

Single constant eddy-viscosity (model A)

In the ground-breaking work by [90] on the dynamics of coherent structures in the turbulent boundary layer, the residual, $g_i(\boldsymbol{a})$, was modelled by a constant 'eddy-viscosity' term, resulting in a linear subscale turbulence representation $g_i(\boldsymbol{a}) = \nu_0^T \sum_{j=1}^{K} l_{ij}^{\nu} a_j$. ν_0^T is generally obtained by solution matching techniques. However, within the work on ROMs in this thesis, the eddy-viscosity is derived from the TKE power balance equation. This equation is obtained by multiplying (3.27) by a_i and averaging over time:

$$\dot{a}_i a_i = \sum_{j=0}^{K} l_{ij}^{\nu} a_i a_j + \sum_{j,k=0}^{K} q_{ijk}^{c} a_i a_j a_k + \nu_0^T \sum_{j=1}^{N} l_{ij}^{\nu} a_i a_j \Rightarrow \tag{3.29a}$$

$$0 = \sum_{j=0}^{K} l_{ij}^{\nu} \langle a_i a_j \rangle + \sum_{j,k=0}^{K} q_{ijk}^{c} \langle a_i a_j a_k \rangle + \nu_0^T \sum_{j=1}^{K} l_{ij}^{\nu} \langle a_i a_j \rangle \Rightarrow \tag{3.29b}$$

$$0 = l_{ii}^{\nu} K_i + \sum_{j,k=0}^{K} q_{ijk}^{c} \langle a_i a_j a_k \rangle + \nu_0^T l_{ii}^{\nu} K_i \Rightarrow \tag{3.29c}$$

$$\nu_0^T = \frac{-l_{ii}^{\nu} K_i - \sum_{j,k=0}^{K} q_{ijk}^{c} \langle a_i a_j a_k \rangle}{l_{ii}^{\nu} K_i} \tag{3.29d}$$

The value of ν_0^T is then found by taking the geometrical average of (3.29d) over $i = 1, ..., K$.

Modal constant eddy-viscosity (model B)

Rempfer and Fasel [92] refined the linear model by reasoning that the eddy-viscosity should be scale-dependent resulting in *modal eddy viscosities* ν_i^T, $i = 1, \ldots, N$. The resulting linear subscale turbulence representation reads $g_i(\boldsymbol{a}) = \nu_i^T \sum_{j=1}^N l_{ij}^\nu a_j$. ν_i^T can be obtained by solution matching. In this study, ν_i^T is derived from the modal power balance [101]:

$$\nu_i^T = \frac{-l_{ii}^\nu K_i - \sum_{j,k=0}^K q_{ijk}^c \langle a_i a_j a_k \rangle}{l_{ii}^\nu K_i} \tag{3.30}$$

Single nonlinear eddy-viscosity (model C)

Noack et al. [95] remark that the subscale turbulence representations of model A and model B are linear while the energy transfer is caused by nonlinear mechanisms. The starting point is a single eddy-viscosity ansatz

$$g_i(\boldsymbol{a}) = \nu_0^T(\boldsymbol{a}) \sum_{j=1}^N l_{ij}^\nu a_j, \tag{3.31}$$

but allow the eddy-viscosity to be state dependent. On the other hand (3.28) is written as

$$g_i(\boldsymbol{a}) = \nu \sum_{j=N+1}^\infty l_{ij}^\nu a_j + \sum_{\substack{j,k=0 \\ max\{j,k\}>N}}^\infty q_{ijk}^c a_j a_k. \tag{3.32}$$

Evidently, both terms cannot be exactly matched. However, the energy transfer rate effect should be similar. In the modal power balance, this energy loss is quantified with $\langle a_i g_i \rangle$. Equality of the energy transfer rate yields

$$\nu^T l_{ii}^\nu \lambda_i = \sum_{\substack{j,k=0 \\ max\{j,k\}>N}}^\infty T_{ijk}, \text{ where } T_{ijk} = q_{ijk}^c \langle a_i a_j a_k \rangle, \tag{3.33}$$

exploiting $\langle a_i a_j \rangle = \lambda_i \delta_{ij}$ (3.15). The triadic power terms on the right-hand side may be approximated with a finite-time thermodynamics closure [96]

$$T_{ijk} = \alpha \chi_{ijk} \sqrt{K_i K_j K_k} \left(1 - \frac{3K_i}{K_i + K_j + K_k} \right). \tag{3.34}$$

In the next step, the relative modal energy contents κ_i are introduced via $K_i = \kappa_i K_\Sigma$, with $\sum_{i=1}^N \kappa_i = 1$. Then, (3.33) becomes

$$2\nu^T l_{ii}^\nu \kappa_i = \sqrt{K_\Sigma} \sum_{\substack{j,k=0 \\ max\{j,k\}>N}}^\infty \alpha \, \chi_{ijk} \sqrt{\kappa_i \kappa_j \kappa_k} \left(1 - \frac{3\kappa_i}{\kappa_i + \kappa_j + \kappa_k} \right). \tag{3.35}$$

This closure relation suggests that ν_T scales with $\sqrt{K_\Sigma}$, assuming that κ_i remain approximately constant with K_Σ. The resulting nonlinear eddy-viscosity model denoted model C thus takes the form:

$$g_i(\boldsymbol{a}) = \nu_0^T \sqrt{\frac{K_\Sigma(t)}{K_\Sigma}} \sum_{j=1}^{N} l_{ij}^\nu a_j. \tag{3.36}$$

Thus, large (small) fluctuation levels $K_\Sigma(t) > K_\Sigma$ ($K_\Sigma(t) < K_\Sigma$) lead to a higher (smaller) damping than predicted by the corresponding linear subscale turbulence representation. In particular, boundedness of the new *Galerkin system C* (GS-C) can be proven, if the energy preservation of the quadratic term is enforced [102].

Modal nonlinear eddy-viscosity

Combining the nonlinear eddy-viscosity of model C (3.36) and the modal eddy viscosities of model B yields the following nonlinear subscale turbulence representation:

$$g_i(\boldsymbol{a}) = \nu_i^T \sqrt{\frac{K_\Sigma(t)}{K_\Sigma}} \sum_{j=1}^{N} l_{ij}^\nu a_j. \tag{3.37}$$

The resulting model is referred to as model D. The value from model A for ν_0^T are used in model C and the values of ν_i^T in model D are taken from the values in model B.

3.2 Cluster-based reduced order modelling (CROM)

CROM is a novel strategy for the systematic charaterisation and reduced-order modelling of unsteady flows suggested by Kaiser et al. [103]. The CROM algorithm partitions the M snapshots into K representative flow states called *clusters*, $\mathcal{C}_k$, with $K < M$. The criterion for assigning a snapshot to each cluster is based on a distance metric between snapshots in the Hilbert space. The distance between two snapshots, $\boldsymbol{u}^m$ and $\boldsymbol{u}^n$, is given by

$$D_{mn} \equiv ||\mathbf{u}^m - \mathbf{u}^n||_\Omega, \tag{3.38}$$

where $||\ ||_\Omega$ corresponds to the norm in Hilbert space (3.5). The clustering algorithm [103] is based on an iterative method where the snapshots firstly are assigned to a random initial distribution of the clusters. The cluster mean, also called the *cluster centroid*, $\boldsymbol{c}_k$, is then defined as the average of all the snapshots belonging to each cluster:

$$\boldsymbol{c}_k = \frac{1}{n_k} \sum_{\mathbf{u}'_m \in \mathcal{C}_k} \mathbf{u}'_m, \tag{3.39}$$

where n_k is the number of snapshots belonging the cluster $\mathcal{C}_k$. The algorithm then iterates and assigns the snapshots to the calculated centroids until convergence is obtained,

based on a minimisation problem of the variances of all clusters. The details are fully outlined in [103]. In addition to the centroids, CROM also provides the Cluster Transition Matrix (CTM) P. The elements P_{jk} in P gives the probability of the flow to move from cluster $\mathcal{C}_k$ to cluster $\mathcal{C}_j$ in one forward time-step. The diagonal elements P_{jj} corresponds to the probability to stay in the cluster $\mathcal{C}_j$ during one time step. The clusters are ordered in such a way that the first cluster $\mathcal{C}_1$ corresponds to the most probable state of the flow, and the second cluster is chosen as the cluster with the highest transition probability to move from $\mathcal{C}_1$ to $\mathcal{C}_2$, and so on. For strictly periodic flows, CROM corresponds to a generalisation of phase averaging.

4 Summary of papers

4.1 Paper A

"The flow around a simplified tractor-trailer model studied by Large Eddy Simulation"

This first paper of the thesis considers aerodynamics of heavy vehicles. Large-eddy simulation (LES) is used to study the flow around a simplified tractor-trailer model. The model consists of two boxes placed in tandem. The front box represents the cab of a tractor-trailer road vehicle and the rear box represents the trailer. The LES was made at the Reynolds number of 0.51×10^6 based on the height of the rear box and the inlet air velocity. Two variants of the model were studied, one where the leading edges on the front box are sharp and one where the edges are rounded. One small and one large gap width between the two boxes were studied for both variants. Two computational grids were used in the LES simulations and a comparison was made with available experimental force measurements. The results of the LES simulations were used to analyze the flow field around the cab and in the gap between the two boxes of the tractor-trailer model. Large vortical structures around the front box and in the gap were identified. The flow field analysis showed how these large vortical structures are responsible for the difference in the drag force for the model that arises when the leading edges on the front box are rounded and the gap width is varied.

4.2 Paper B

"LES Study of breakdown control of A-pillar vortex"

In this paper, a passenger vehicle flow is considered. A longitudinal vortex, called the A-pillar vortex, is formed along the side wind screens of passenger cars. This vortex is responsible for induced drag on the vehicle due to the momentum transferred from the moving vehicle to the air entrapped in the vortex. It is also the main contributor to in-cabin noise for the passenger inside the vehicle as well as dirt and water distribution on the side of the car. These kinds of longitudinal vortices are in themself extremely complex flow phenomenons. Their most familiar occurence is maybe on the suction side on the delta wing. They undergo a phenomen called "vortex breakdown", which is characterized by a sudden decrease in the axial flow and stagnation of the flow inside the core, as well as rapid increase in the pressure inside the core and a decrease in the tangential velocity. In this paper, active flow control of the longitudinal vortices were studied using LES. The LES results were validated against existing Particle Image Velocitimetry (PIV) and aerodynamic drag data. The LES results were further used to study the flow physics responsible for the development of the longitudinal vortex, in particular the vortex breakdown process. Tangential blowing and suction into the separating shear layer forming the longitudinal vortex was found to be a sensitive process that can cause instabilities in the flow. The resulting LES flows also show that actuation influences not only the

longitudinal vortex nearest to the actuation slot but also the overall flow. Thus, the influence of the flow control acuation on the entire flow must be considered in order to be able to find the apporpriate level of control for optimal aerodynamic performance.

4.3 Paper C

"Simulations of flow around a simplified train model with a drag reducing device using Partially Averaged Navier-Stokes"

This paper examines the flow around a regional train model with similar rectangular geometrical features as the Bombardier Contessa train which is used in Sweden. The train model has previously been studied in wind tunnel experiments [104] and has a length to height/width ratio of 7:1. The Reynolds number based on the height of the train model is $0.37 \cdot 10^6$. For this Reynolds number, the flow separates from the curved leading edges on the front then attaches again on the roof and sides forming a boundary layer there before separating in the wake. The high Reynolds number and the length of the train makes the flow around it a difficult task to predict. It is unfeasible to make an accurate and well resolved LES simulation of the flow around it. Therefore, the recently developed hybrid turbulence technique Partially Averaged Navier Stokes (PANS) was choosen. The objective for the research in this paper is two-fold. The first objective is to evaluate PANS for this kind of vehicle aerodynamic flows and the second objective is to decrease the drag on the train model by some add-on device. The add-on device that was choosen was an open cavity placed at the base of the train model. Even though this might not be the most practically construction for a real train, the device was choosen in order to get a starting point for further investigations later on. Two cases of the flow around the train model were simulated in the paper. The first case is of the natural flow around the train model where direct comparison to experimental data of drag coefficient and pressure coefficient are made. In the second case an open cavity is placed on the base of the train model with the aim of reducing the overall drag on the model. The results show that the drag for model with the cavity is reduced by some 10% compared to the drag of the natural case. The agreement to experimental data for the natural case is not perfect but the general features in the flow field are simulated correctly.

4.4 Paper D

"A study of the aerodynamics of a generic container freight wagon using Large-Eddy Simulation"

The focus of the work in this paper is entirely dedicated to the physics of the unsteady flow around a container freight wagon. Therefore, the well-known and established method of LES with the Standard Smagorinsky model was used as in the previous papers. The generic container freight wagon model consists of one 11.8 m standard container placed on a wagon. Details on the undercarriage such as wheels are included, but the model is generic and smoothed in comparison to a real freight wagon. This model has

not been investigated experimentally in wind tunnel by us or any other researchers previously. Therefore, a fairly low Reynolds number was choosen and two grids which both provided excellent spatial resolution were constructed in order to get reliable results. An examination of the flow close to the surface on the container's roof revealed that even low and high speed streaks were resolved in a plane located 5 viscous units from the wall. The choosen Reynolds number of the flow was 10^5 based on the width of the container. A previous experimental study [105] of the flow around one double-stacked container freight wagon has shown that the drag coefficient obtains self similarity for Reynolds numbers above approximately $0.8 \cdot 10^5$. The results recorded from the simulations were used to analyse and describe both the mean and the instantaneous flow around the wagon. The flow around the front was found to be dominated by regions of massive separated flow. The flow beneath the wagon was found to be irregular and chaotic.

4.5 Paper E

"On the need for a nonlinear subscale turbulence term in POD models as exemplified for a high Reynolds number flow over an Ahmed body"

This paper presents a ROM for the flow around the vehicle-like bluff body called Ahmed body. The input to the ROM is a dataset of spatially and temporally resolved flow snapshots produced by an LES simulation. The Reynolds number in the study is 300 000 which makes it challenging for any ROM due to the coherent structures and the broadband frequency of the turbulence scales in the wake. Moreover, the flow around this body was found in the recent experimental study by Grandemange et al. [106] to inhibit a bi-modal behavior in the wake, where the flow switches from one assymmetric state to the other over time scales ranging between 100-1000 convective time units. The LES simulation of the present study predicts this bi-modal behavior as well. In this study, different sub-scale closures for the ROM was investigated. The ROMs are found to be most accurate with modal eddy viscosities as proposed by Rempfer & Fasel (1994). Robustness of the model solution with respect to initial conditions, eddy viscosity values and model order is only achieved for state-dependent eddy viscosities as proposed by Noack, Morzyński & Tadmor (2011). Only the POD system with state-dependent modal eddy viscosities can address all challenges of the flow characteristics. All parameters are analytically derived from the Navier-Stokes based balance equations with the available data. We arrive at simple general guidelines for robust and accurate POD models which can be expected to hold for a large class of turbulent flows.

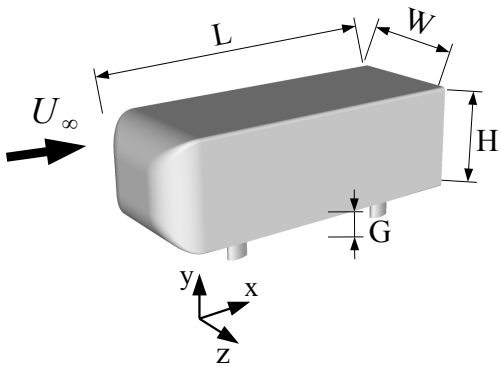

Figure 5.1: The Ahmed body model, square back configuration.

5 Results

This chapter presents some additional results that are not already presented in the appended papers. In section 5.1 the results from a POD decomposition of a set of flow snapshots in the wake of a 3D-bluff body are presented. In section 5.1.4, the results from a CROM analysis of the same snapshot database is outlined.

5.1 Reduced-Order Modelling of the Ahmed body wake, $\mathbf{Re = 300\,000}$

This section presents analysis from POD and CROM of the Ahmed body wake. The Ahmed model [107] (see figure 5.1) is used in vehicle aerodynamics as a generic test case that reproduces the important flow structures around passenger vehicles [108, 109]. Recently, the model has been subjected to intensive research for the pursuit of flow control methods capable of reducing the aerodynamic drag on the model, both passive control [110, 111], and actuation control [113, 115, 114, 112]. In this thesis, the focus is on the square-back variant of the Ahmed body, which is essentially a blunt body with curved front edges placed in the proximity of ground. Similar bodies have been studied numerically by Krajnović and Davidson [116], Khalighi et al. [117] and Verzicco et al. [118]. The recent experimental investigations by Grandemange et al. [119] have shown that the organization of the flow in the wake is strongly dependent on the ground clearance, G, between the body and the ground. For ground clearances of $0 < G < 0.05\,H$, the flow in the wake behaves as the flow behind a back-ward facing step, thus preventing the underbody flow to gain momentum. For $0.05\,H < G < 0.09\,H$, the flow under the body has higher momentum, but the adverse pressure gradient after the separation bubble behind the wake makes the flow coming from underneath the body to separate on the ground. For $G > 0.09\,H$, the momentum of the flow underneath the body is high enough

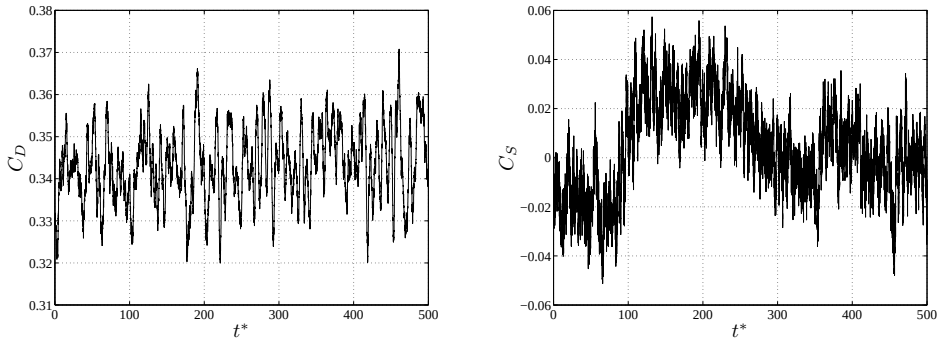

a) b)

Figure 5.2: Time history of the force signals from the LES simulation. a) drag force; b) side force.

to prevent the separation on the ground due to the adverse pressure gradient. In the present study, the ground clearance is $G = 0.17\,H$. The study by [106] has shown that the flow exhibits a bi-stability in the lateral direction. The flow switches from one bi-stable anti-symmetric state on one side to the other side randomly, making the flow in the wake statistically symmetric. The shift of these bi-stable states occurs over large time scales of the order of $T \sim 10^3 - 10^4 H/U_\infty$. The presence of the bi-stable states have been found from Reynolds numbers ranging from $Re \sim 10^2$ to $Re \sim 10^6$ [120, 106]. It was also observed in these studies that the time-scale of the shift between the bi-stable antisymmetric states decreases with increased Reynolds number.

5.1.1 Dataset of flow snapshots

The observation region $\Omega_{POD} \subset \Omega$ is a wake centred subset of the computational domain

$$\Omega_{POD} = \{(x, y, z) \in \Omega : \; 0 \leq x \leq 20\,H, -0.67\,H \leq y \leq 1.12\,H, |z| \leq 1.21\,H.\} \qquad (5.1)$$

1000 snapshots covering 500 convective time units ($t^* = tU_\infty/H$) are obtained from an LES simulation. Another 1000 mirror-symmetric (with respect to the z-axis) snapshots are then included in the database, so that it consists of $M = 2000$ snapshots in total and covers 1000 convective units. The details of the LES simulation and a validation of the LES results to experimental data can be found in Paper E (*"On the need for a nonlinear subscale turbulence term in POD models as exemplified for a high Reynolds number flow over an Ahmed body"*) in this thesis.

5.1.2 LES results

Figure 5.2a) presents the time history of the normalized drag force signal, C_D, from the LES simulation. A spectral analysis of the signal reveals several low frequency peaks at Strouhal numbers $St = t \cdot H/U_\infty = 0.036$, 0.054, 0.085, 0.12, 0.17 and 0.21, but no dominating peak is found, indicating a broad band spectrum of the flow structures in the

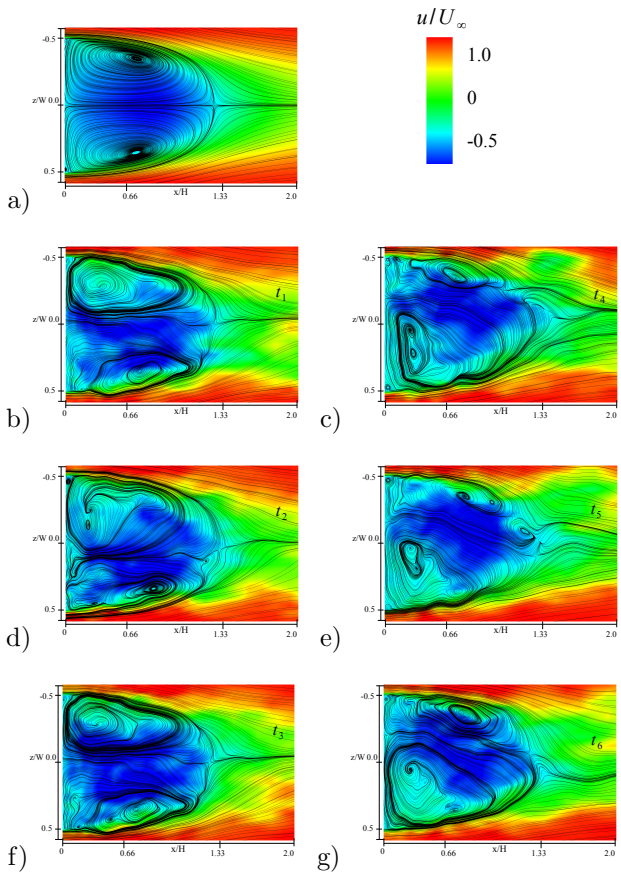

Figure 5.3: Visualizations of the wake flow.

wake. Figure 5.2b) shows the side force signal, C_S. The shift from one bi-modal state to the other is clearly indicated in the side force signal.

The flow in the horizontal plane in the wake is visualized in figure 5.3. Figure 5.3a) shows the mean flow over all of the $M = 2000$ snapshots. Figures 5.3a),d) and f) shows three consecutive time-steps of the instantaneous flow starting at $t_1 = 50t^*$. Here, the flow is in one of the bi-modal states. Figures 5.3c),e) and g) show three time steps in a similar manner when the flow is in the other bi-modal state, starting at $t_4 = 150t^*$.

5.1.3 POD

The spectrum of the POD decomposition is presented in figure 5.4. The energy distribution of the modes show a broad band character. The first 100 modes contain $\sim 35\%$ of the total kinetic energy, and the first 1000 modes contain approximately 80% of the total

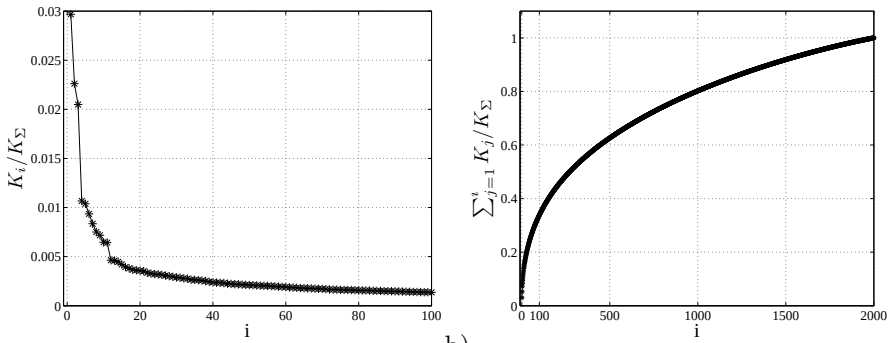

Figure 5.4: Spectrum from the full POD: a) Normalized spectrum; b) Normalized cumulative spectrum.

energy. The first mode contain 3% of the total kinetic energy. This mode will be seen to correspond to the shift mode from one bi-modal state to the other.

The first 10 POD modes are presented in figures 5.5 and 5.5 together with their amplitude. The first mode in 5.5a) can be identified to correspond to a shift mode for the bi-modal states. The amplitude of the first mode, $a_1(t)$, is seen to correspond well with the side force signal in figure 5.2b).

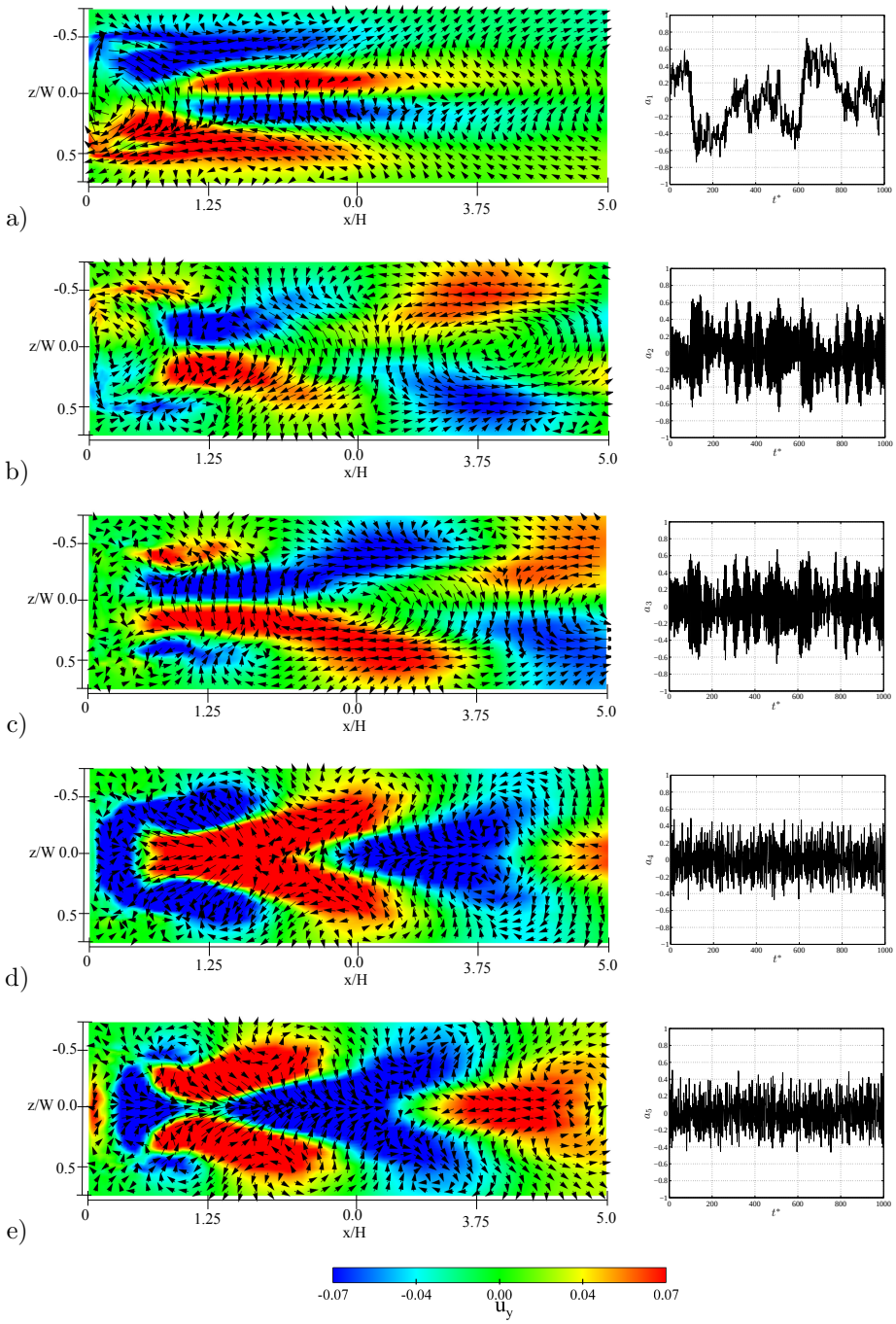

Figure 5.5: Modes from the POD of the full snapshots database .a) Mode 1; b) Mode 2; c) Mode 3; d) Mode 4; Mode 5.

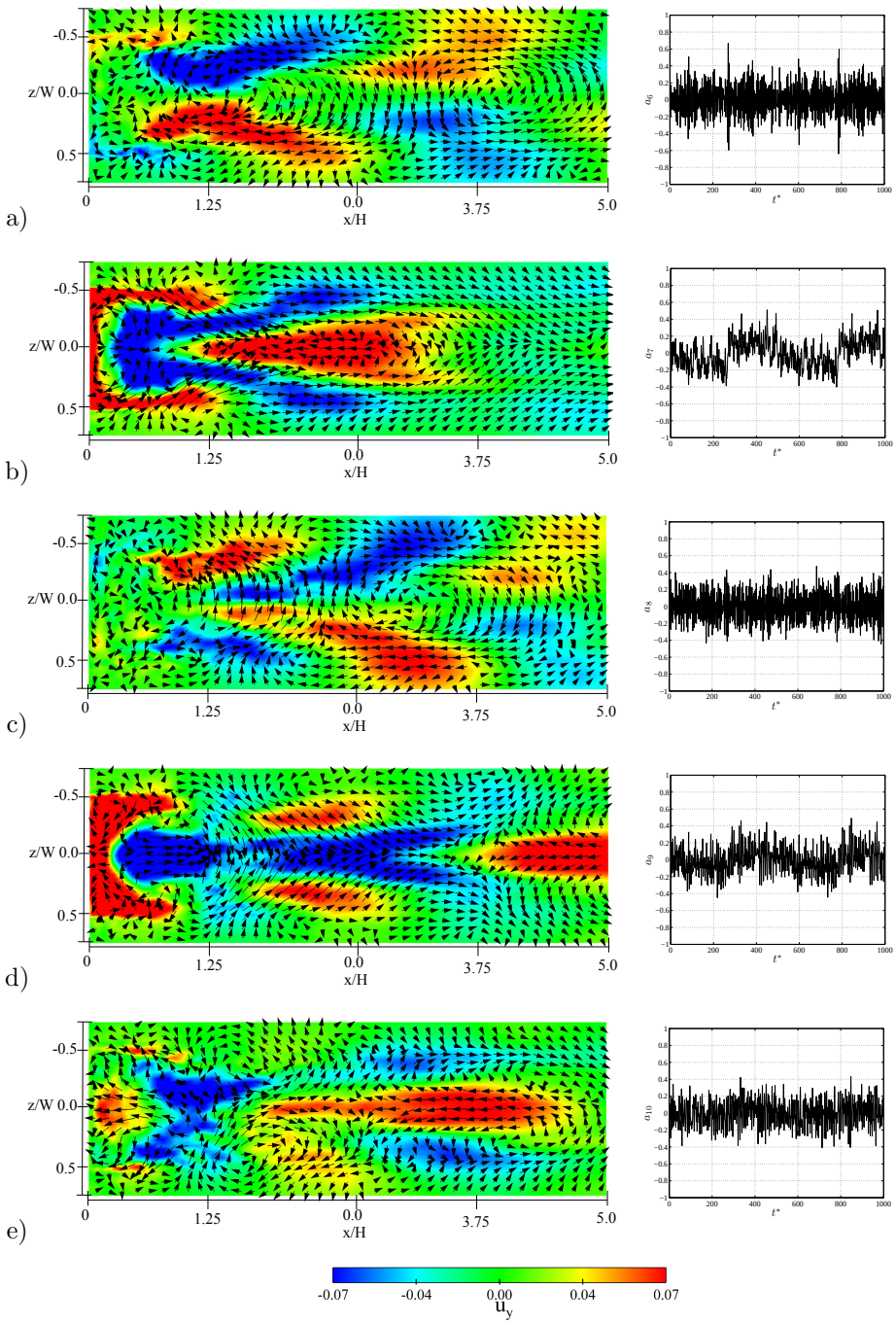

Figure 5.6: Modes from the POD of the full snapshots database .a) Mode 6; b) Mode 7; c) Mode 8; d) Mode 9; e) Mode 10.

5.1.4 CROM

In this section, results from the CROM analysis (see section 3.2) are presented. An instantaneous realisation of an iso-surface of the second invariant of the velocity gradient tensor $Q = -\frac{1}{2}\frac{\partial \overline{u_i}\partial \overline{u_j}}{\partial x_i \partial x_j}$ colour-marked by the pressure coefficient is shown in figure 5.7.

All results below are visualised with regard to the horizontal plane $y = 0$ as displayed in figure 5.7b). The cluster analysis is performed in the full POD space for $K_c = 10$ clusters. The distance matrix is visualised in figure 5.8(a) displaying three groups of clusters. Two groups, namely clusters $k = 5, 6, 7$ ('B1') and $k = 8, 9, 10$ ('B2'), are comparably far away from each other, while they are equally close to the group of clusters $k = 1, 2, 3, 4$ ('T').

Moreover, these groups are characterised by an intrinsic periodical behaviour as concluded from the cluster transition matrix (see figure 5.8(b)). Similar to the mixing layer, high probabilities in the first sub diagonal and a closing transition from the last cluster to the first cluster inside the group indicate a periodical oscillation. While the groups 'B1' and 'B2' show nearly no connectivity, the group 'T' serves as a transition region between them. The most significant transitions are $3 \rightarrow 7$ (T $\rightarrow$ B1) and $2 \rightarrow 8$ (T $\rightarrow$ B2) as well as $5 \rightarrow 1$ (B1 $\rightarrow$ T) and $8 \rightarrow 4$ (B2 $\rightarrow$ T). The cluster centroids computed as the mean of the velocity fluctuations in each cluster are displayed in figure 5.9.

The clusters in 'B1' and 'B2' are characterised by strong vortical structures in opposite direction resembling the two semi-modal flow states. Cluster $k = 5$ is an exception which is addressed below. The strength of the clusters in 'T' is weaker and the vector fields seem to be more symmetric with regard to the centerline $z = 0$. The principal branching clusters are $k = 5$ and $k = 8$ connecting group 'T' with 'B1' and 'B2', respectively. These are intermediate states which explains why $k = 5$ seems more similar to the states in 'T' and $k = 8$ shares more dominant features with 'B2'.

An intuitive picture of the cluster transitions and the corresponding states is provided in figure 5.10.

The simplified cluster transitions are displayed in figure 5.10 (a). The large cluster group 'T' connects the two semi-modal states characterised by 'B1' and 'B2'. Clusters $k = 5$ and $k = 8$ have a special role and serve as branchig clusters. Apparently, the plots of the mean of each cluster group (figure 5.10 (b-d)) confirms that 'B1' and 'B2' represent the two asymmetric states while 'T' represents a low-amplitude oscillation around the

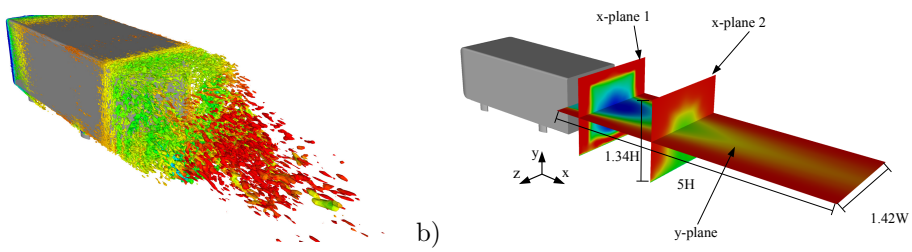

Figure 5.7: Bluff body wake: a) Instantaneous iso-surface of $Q = 150000$ which is coloured by the pressure coefficient $c_p = \Delta p / \frac{1}{2}\rho U_\infty^2$ with $\Delta p = p - p_\infty$ where p_∞ is the pressure in the freestream. The wake is characterised by a broadband spectrum exhibiting no obvious large-scale structures. b) Plane used to visualize results.

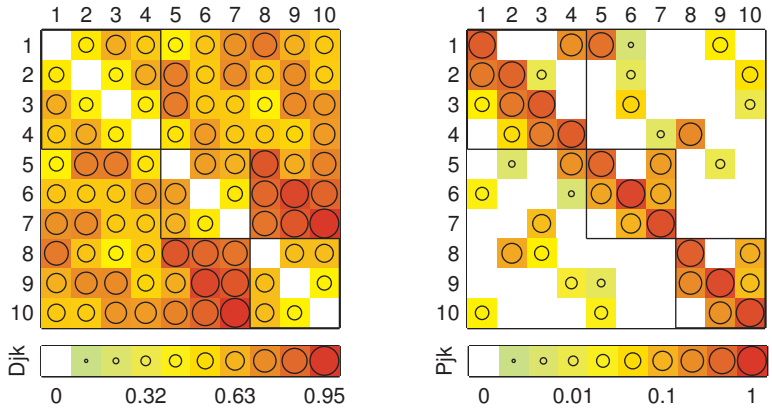

Figure 5.8: Kinematics and dynamics: Three groups of clusters are distilled, namely groups 'T' ($k = 1, 2, 3, 4$), 'B1' ($k = 5, 6, 7$), and 'B2' ($k = 8, 9, 10$).

symmetric base flow (figure 5.10 (c)).

A further analysis of the forces reveals that the two semi-modal states are associated with an increase in the side forces which was also found by [106] and [58] for the same data. In figure 5.11 the Voronoi diagram of the clusters, the cluster centroids (coloured bullets), and the data points (coloured dots) are displayed.

The mean forces associated with each cluster are shown as bar plots of which the first bar corresponds to the drag coefficient $C_D = F_x/(\frac{1}{2}\rho U_\infty HW)$, the second to the lift cooefficient $C_L = F_y/(\frac{1}{2}\rho U_\infty HW)$, and the third to the side force coefficient $C_S = F_z/(\frac{1}{2}\rho U_\infty HW)$. While the drag and the lift do not show any significant drift, the side force coefficient changes signs when the flow switches from one side to another. The lowest values in magnitude correspond to the clusters in 'T' which is consistent since they are tendentially symmetric.

Finally, the spectrum of the CTM displayed in figure 5.12 is analysed.

Figure 5.12 displays the real and imaginary part of $\mu = 1/\Delta t \log(\lambda)$ where λ is an eigenvalue of the CTM as defined in section 3.2. This transformation yields the growth rates and frequencies of the corresponding probability eigenvectors which can be directly linked to the growth rates and frequencies of observables, e.g. velocity field or pressure measurements. Besides the invariant distribution corresponding to $\lambda = 1$, there exist three oscillatory modes. The frequency of the oscillatory mode with the smallest damping is $St = \omega_4/2\pi \approx 0.17$ (displayed in red bullets) close to $St = 0.2$ of the global wake shedding. Note that the oscillations are only resolved by 3 or 4 clusters. Better estimations can be obtained by a refined resolution, i.e. increasing the number of clusters K.

In summary, CROM distills the two bi-modal states of the base flow and identifies the main transition mechanism. These asymmetric quasi-attractors are connected to the comparably symmetric transition region solely via the two branching clusters $k = 5$ and $k = 8$. All groups are intrinsically periodic and the dominant frequency is determined as

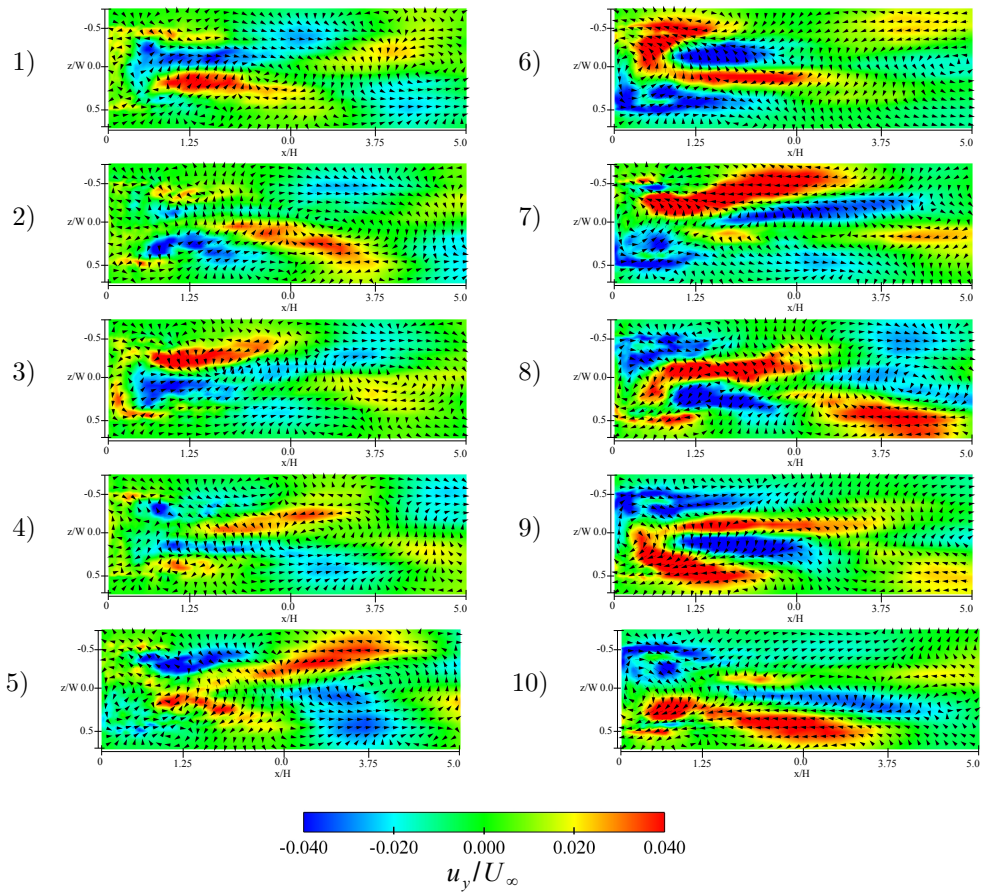

Figure 5.9: Cluster centroids of the Ahmed body. Visualisations of the $y-$planes coloured by u_y/U_∞. Cluster group 'T' ($k = 1, 2, 3, 4$) resembles the symmetric transition region, cluster groups 'B1' ($k = 5, 6, 7$) and 'B2' ($k = 8, 9, 10$) represent the two semi-modal asymmetric states.

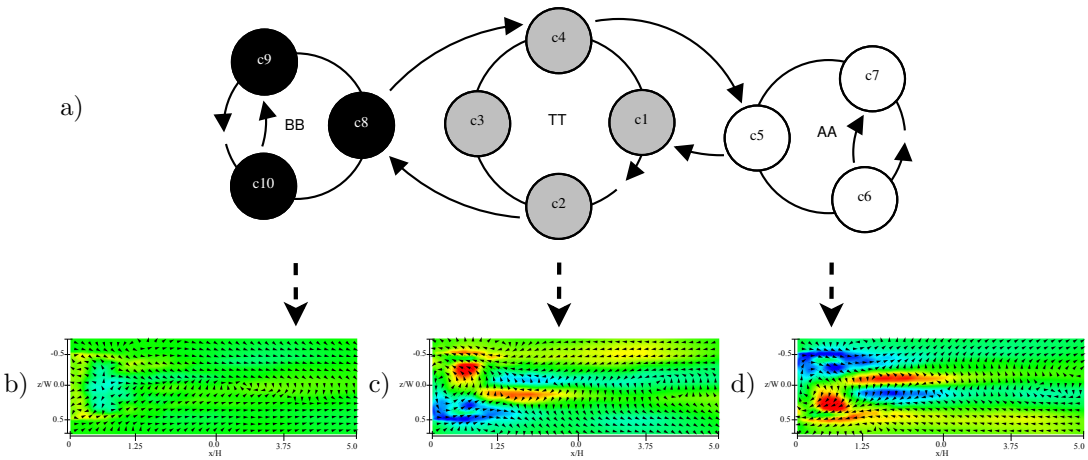

Figure 5.10: Simplified cluster transitions. The arrows indicate possible transitions above a certain threshold. This threshold is chosen small enough to guarantee full connectivity. The graph highlights three cyclic groups associated with the two asymmetric meta-stable states and a transition region between them. Two branching clusters, $k = 5$ and $k = 8$, connect these groups. Mean velocity fields of the three cluster groups of Ahmed body are shown below: (b) bi-modal group 'B2' of clusters $k = 8, 9, 10$, (c) symmetric group 'T' of clusters $k = 1, 2, 3, 4$, (d) bi-modal group 'B1' of clusters $k = 5, 6, 7$. The visualisation of the mean flows corresponds to those in figure 5.9.

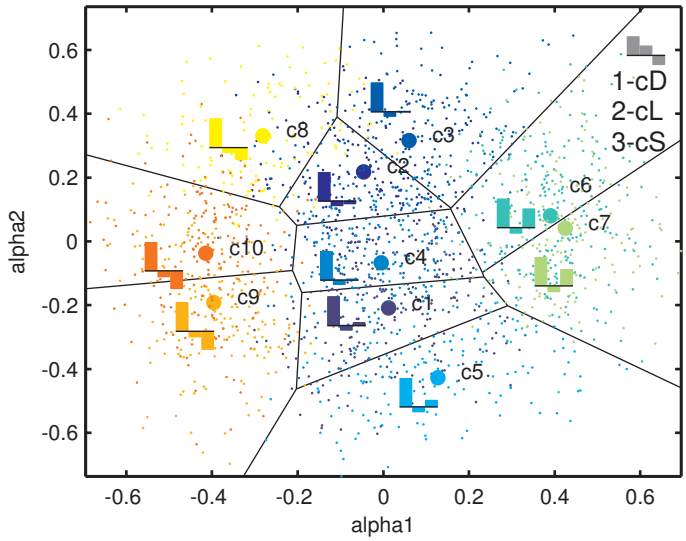

Figure 5.11: Cluster forces of the Ahmed body: Visualisation of the Voronoi diagram of the clusters, the cluster centroids (coloured bullets), the data points (coloured dots), and bar plots of the mean force-related coefficients of each cluster in the space of the first two POD modes α_1 and α_2 associated with the centroids. The coefficients are normalised with respect to the drag coefficient. The side coefficient is $\times 10$ enlarged for visualisation purposes. The colours indicate the different clusters. The clusters associated with the largest side forces correspond to the outer clusters $k = 5, 6, 7$ and $k = 8, 9, 10$, respectively, which represent the two asymmetric flow states.

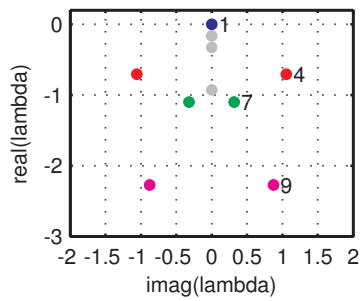

Figure 5.12: Stability analysis of the transition matrix associated with the Ahmed body: The growth rate $\sigma = \Re(\mu)$ and the frequency $\omega = \Im(\mu)$ are shown according to the transformation $\mu = 1/\Delta t \log(\lambda)$. The marginal stable eigenvalue μ_1, or $\lambda = 1$, has vanishing growth rate and frequency (blue bullet) and is associated with the asymptotic probability distribution. Other non-oscillatory modes are visualised with grey bullets. The frequency corresponding to the oscillatory mode with the smallest damping (red bullets) is $St \approx 0.17$.

$St = 0.17$. A larger number of clusters increases the resolution of the bi-stable states and the branching clusters but not change the main mechanism.

6 Concluding remarks

The focus of the work presented in this thesis is on the numerical simulations of the flow around vehicles. The flow around simplified passenger cars, tractor-trailers and trains has been considered. Two differents unsteady methods have been used in the simulations, the primary being Large Eddy Simulations. This method was used to study the flow around a tractor-trailer in paper A, the breakdown of the swirling longitudinal A-pillar vortex along the sides of a simplified passenger car model in paper B, the flow around a freight wagon in paper D and the flow around a square-back passenger car model in paper E. The Standard Smagorinsky subgrid model has been used in the Large Eddy Simulations. Although simple, this model has proven to be very capable of producing reliable solutions of flow fields. In all of the simulations, the employed computational grids have been carefully constructed block-structured grids, and the key for successful results is that a sufficient spatial resolution is obtained by the grids. Since a physical representation of the flow is highly dependent on the spatial resolution, the computational costs of the simulations limits the Reynolds numbers that can be achieved with LES. A remedy for this can be to use less accurate hybrid/zonal models, such as the Partially-Averaged Navier Stokes which is the second unsteady model that was used in this work. That model was used to study the flow around a simplified regional train model in paper C.

In addition to the simulations and the analysis of the flow around the vehicles, Reduced-Order Modelling was explored in paper E of the thesis. Reduced Order-Modelling in the context of fluid dynamics consists in simplifiying the governing Navier-Stokes equation to a reduced set of equations. One way to do this is by the decomposition of the flow field into spatial stationary modes with corresponding time-dependent amplitudes. Inserting this decomposition into the Navier-Stokes equations yields a dynamical system. If a method that yields orthogonal modes are used, such as the Proper Orthogonal decomposition, the resulting reduced equations consist of a coupled quadratic-linear system of equations for the amplitudes. In the work in this thesis, different closure methods for such reduced system were explored for the high Reynoldsnumber flow in the wake of a square back vehicle model. Additional results presented in the extended abstract of the thesis concerns another method of obtaining a Reduced-Order model, the recently proposed method of Cluster-Based Reduced-Order Modelling.

References

[1] M. Zdravkovich. *Flow Around Circular Cylinders, Volume 1: Fundamentals*. Oxford, New York, Tokyo: Oxford University Press, 1997.

[2] R. Panton. *Incompressible Flow*. third edition. New York, etc.: John Wiley & Sons, 2005.

[3] F. Champagne, Y. Pao, and I. Wygnanski. On the two-dimensional mixing region. *J. Fluid Mech.* **74** (1976), 209–250.

[4] W.-H. Hucho. *Aerodynamics of Road Vehicles*. 4th ed. ISBN 0-7680-0029-7. Society of Automotive Engineers, Inc., 1998.

[5] J. Östh and S. Krajnović. The flow around a simplified tractor-trailer model studied by Large Eddy Simulation. *J. Wind. Eng. Ind. Aerod.* **102** (2012), 36–47.

[6] S. Krajnović, J. Östh, and B. Basara. LES Study of breakdown control of A-pillar vortex. *Int. J. Flow Control* **2**.4 (2010), 237–257.

[7] S. Krajnović and L. Davidson. Flow around a simplified car, part 1: large eddy simulation. *J. Fluid. Eng.-T ASME* **127** (2005), 907–918.

[8] S. Krajnović and L. Davidson. Flow around a simplified car, part 2: understanding the flow. *J. Fluid. Eng.-T ASME* **127** (2005), 919–928.

[9] S. Krajnović, J. Östh, and B. Basara. "LES of active flow control around an Ahmed body with Active Flow Control". *Conference on Modelling Fluid Flow (CMFF'09), The 14th International Conference on Fluid Flow Technologies*. Budapest, Hungary, 9-12 September, 2009.

[10] F. Alam, S. Watkins, and G. Zimmer. Mean and time-varying flow measurements on the surface of a family of idealized road vehicles. *Exp. Therm. Fluid Sci.* **27** (2003), 639–654.

[11] G. I. Figura-Hardy. 2007 RSSB Slipstream Safety - Analysis of existing experimental data on train slipstreams including the effects on pushchairs. *Rail Safety and Standards Board* (2007).

[12] M. Sterling, C. J. Baker, S. C. Jordan, and T. Johnson. A study of the slipstreams of high-speed passenger trains and freight trains. *Proc. Inst. Mech. Eng. F J. Rail Rapid Transit* **222** (2008), 177–193.

[13] T. W. Muld. "Slipstream and Flow Structures in the Near Wake of High-Speed Trains". ISBN/ISSN 978-91-7501-392-3. PhD thesis. Stockholm, Sweden: Royal Institute of Technology, 2012.

[14] H. Hemida, N. Gil, and C. Baker. LES Study of the slipstream of a rotating train. *J. Fluid. Eng.-T ASME* **132** (2010), pages.

[15] H. Hemida. "Numerical Simulations of Flows around Trains and Buses in Cross Winds". ISBN/ISSN 978-91-7385-187-9. PhD thesis. Gothenburg, Sweden: Chalmers University of Technology, 2008.

[16] S. Krajnović, P. Ringqvist, K. Nakade, and B. Basara. Large Eddy Simulation of the flow around a simplified train moving through a crosswind flow. *J. Wind. Eng. Ind. Aerod.* **110** (2012), 86–99.

[17] H. Kim. Aerodynamic analysis of a train running in a tunnel. *Korean Soc. Mech. Eng. (KSME)* **21(8)** (1997), 963–72.

[18] A. E. Vardy. Aerodynamic drag on trains in tunnels. 1. Synthesis and definitions. *Proc. World Congr. Inst. Mech. Eng.* **210** (1996), 29–38.

[19] A. E. Vardy. Aerodynamic drag on trains in tunnels. 2. Prediction and validation. *Proc. World Congr. Inst. Mech. Eng.* **210** (1996), 39–49.

[20] D. Heine and K. Ehrenfried. "Experimental Study of the Compression-Wave Generation due to Train-Tunnel Entry". *Proceedings of the First International*

Conference on Railway Technology: Research, Development and Maintenance. Ed. by J. Pombo. Civil-Comp Press, Stirlingshire, Scotland, paper 163, 2012.

[21] R. S. Raghunathan, H.-D. Kim, and T. Setoguchi. Aerodynamics of high-speed railway train. *Prog. Aerosp. Sc.* **38** (2002), 469–514.

[22] D. Uystepruyst, W.-L. Mame, E. Creuśe, and S. Nicaise. Efficient 3D numerical prediction of the pressure wave generated by high-speed trains entering tunnels. *Comp. Fluids* **47** (2011), 165–177.

[23] M. Jönsson, C. Wagner, and S. Loose. "High-speed particle image velocimetry of the underfloor flow of a generic high-speed train model". *Proceedings of the First International Conference on Railway Technology: Research, Development and Maintenance*. Ed. by J. Pombo. Civil-Comp Press, Stirlingshire, Scotland, paper 153, 2012.

[24] W. King III. A précis of developments in the aeroacoustics of fast trains. *J. Sound Vib* **193** (1996), 349–358.

[25] W. J. Davis. The tractive resistance of electric locomotives and cars. *Gen. Electr. Rev.* **29** (1926), 2–24.

[26] P. Lukaszewicz. Running resistance - results and analysis of full-scale tests with passenger and freight trains in Sweden. *Proc. Inst. Mech. Eng. F J. Rail Rapid Transit* **221** (2006), 183–193.

[27] B. P. Rochard and F. Schmid. A review of methods to measure and calculate train resistances. *Proc. Inst. Mech. Eng. F J. Rail Rapid Transit* **214** (2000), 185–199.

[28] P. Lukaszewicz. "Energy Consumption and Running Time for Trains". PhD thesis. Stockholm, Sweden: Royal Institute of Technology, 2001.

[29] R. Engdahl. "Full-scale rail car testing to determine the effect of position-in-train on aerodynamic resistance". *Publication R-705*. Association of American Railroads, 1987.

[30] R. Engdahl, G. R.L., and J. C. Paul. "Train resistance - aerodynamics Volume II, Open top car application". *Proc., Railroad Energy Technology Conference II*. Atlanta, GA.: Association of American Railroads, 1986, pp. 225–242.

[31] S. Hoerner. "Efficiency of Railroad Trains". *Fluid Dynamic Drag*. Hoerner Fluid Dynamics, Brick Town, New Jersey, 1965, pages.

[32] Johansen. Air Resistance of Trains. *Proc. Institute Mech. Engineers* **134** (1936), p.91.

[33] A. Orellano and S. Sperling. "Aerodynamic Improvements and Associated Energy Demand Reduction of Trains". *The Aerodynamics of Heavy Vehicles II: Trucks, Buses, and Trains*. Vol. 41. Springer Berlin / Heidelberg, 2009, pp. 219–231.

[34] J. Östh and S. Krajnović. "Simulations of flow around a simplified train model with a drag reducing device using Partially Averaged Navier-Stokes". *Conference on Modelling Fluid Flow (CMFF'12), The 15th International Conference on Fluid Flow Technologies*. Budapest, Hungary, 4-7 September, 2012.

[35] J. Östh and S. Krajnović. A study of the aerodynamics of a generic container freight wagon using Large-Eddy Simulation. *J. Fluid. Struct.* **44** (2014), 31–51.

[36] S. B. Pope. *Turbulent Flows*. first edition. Cambridge: Cambridge University Press, 2000.

[37] R. Ecke. The Turbulence Problem: An Experimentalist's Perspective. *Los Alamos Science* **29** (2005), 124–141.
[38] J. Lumley. *Stochastic Tools in Turbulence*. New York: Academic Press, 1970.
[39] R. J. Adrian. Hairpin vortex organization in wall turbulence. *Phys. Fluids* **19** (2007), 041301.
[40] S. J. Kline, W. C. Reynolds, F. A. Schraub, and R. P. W. The structure of the turbulent boundary layer. *J. Fluid Mech.* **30** (1967), 741–773.
[41] C. R. Smith and S. P. Metzler. The characteristics of low-speed streaks in the near-wall region of a turbulent boundary layer. *J. Fluid Mech.* **129** (1983), 27–54.
[42] C. R. Doering. The 3D Navier-Stokes Problem. *Ann. Rev. Fluid Mech.* **41** (2009), 109–128.
[43] A. Kolmogorov. The local structure of turbulence in incompressible viscous fluid for very large Reynolds number. *Dokl. Akad. Nauk SSSR* **30** (1941). (translated and reprinted 1991 in Proc. R. Soc. Lond. A **434**, 9–13), 9–13.
[44] A. Kolmogorov. On degeneration (decay) of isotropic turbulence. *Dokl. Akad. Nauk SSSR* **31** (1941), 538–540.
[45] A. Kolmogorov. Dissipation of energy in locally isotropic turbulence. *Dokl. Akad. Nauk SSSR* **32** (1941). (translated and reprinted 1991 in Proc. R. Soc. Lond. A **434**, 15–17), 16–18.
[46] S. Kurien and M. A. Taylor. Direct Numerical Simulations of Turbulence: Data generation and statistical Analysis. *Los Alamos Science* **29** (2005), 143–151.
[47] T. Ishihara, T. Gotoh, and Y. Kaneda. Study of High-Reynolds Number Isotropic Turbulence by Direct Numerical Simulation. *Ann. Rev. Fluid Mech.* **41** (2009), 165–180.
[48] T. Ishihara, Y. Kaneda, M. Yokokawa, K. Itakura, and A. Uno. Small-scale statistics in high-resolution direct numerical simulation of turbulence: Reynolds number dependence of one-point velocity gradient statistics. *J. Fluid Mech.* **592** (2007), 335–366.
[49] P. Schlatter and R. Örlü. Assessment of direct numerical simulation data of turbulent boundary layers. *J. Fluid Mech.* **659** (2010), 116–126.
[50] X. Wu, J. R. Baltzer, and R. J. Adrian. Direct numerical simulation of a 30R long turbulent pipe flow at $R^+ = 685$: large- and very large-scale motions. *J. Fluid Mech.* **698** (2012), 235–281.
[51] P. Sagaut. *Large Eddy Simulation for Incompressible Flows*. Third ed. Springer, 2006. ISBN: 3-540-26344-6.
[52] J. Smagorinsky. General circulation experiments with the primitive equations. *Monthly Weather Review* **91**.3 (1963), 99–165.
[53] S. Krajnović. LES of Flows Around Ground Vehicles and Other Bluff Bodies. *Phil. Trans. R. Soc. A* **367**.1899 (2009), 2917–2930.
[54] S. Krajnović. "Large-Eddy Simulation for Computing the Flow Around Vehicles". ISBN/ISSN 91-7291-188-3. PhD thesis. Gothenburg, Sweden: Chalmers University of Technology, 2002.
[55] E. Wassen and F. Thiele. Road Vehicle Drag Reduction by Combined Steady Blowing and Suction. *AIAA Paper 2009-4174*. (2009).

[56] S. Ghosal and P. Moin. The Basic Equations for the Large Eddy Simulation of Turbulent Flows in Complex Geometry. *J. Comput. Phys.* **118** (1995), 24–37.

[57] J.-L. Guermond, J. T. Oden, and S. Prudhomme. Mathematical Perspectives on Large Eddy Simulation Models for Turbulent Flows. *J. Math. Fluid Mech.* **6** (2 2004), 194–248.

[58] J. Östh, B. R. Noack, S. Krajnović, D. Barros, and J. Borée. On the need for a nonlinear subscale turbulence term in POD models as exemplified for a high Reynolds number flow over an Ahmed body. *J. Fluid Mech.* **747** (2014), 518–544.

[59] S. S. Girimaji. Partially-Averaged Navier-Stokes Model for Turbulence: A Reynolds-Averaged Navier-Stokes to Direct Numerical Simulation Bridging Method. *J. Appl. Phys.* **73** (2006), 413–421.

[60] M. R. Khorrami, B. Singer, and M. E. Berkman. Time-accurate simulations and acoustic analysis of slat free shear layer. *AIAA Journal* **40** (2002), 1284–1291.

[61] S. S. Girimaji, E. Jeong, and R. Srinivasan. Partially-Averaged Navier-Stokes Method for Turbulence: Fixed Point Analysis and Comparison With Unsteady Averaged Navier-Stokes. *J. Appl. Phys.* **73** (2006), 422–428.

[62] M. Germano. Turbulence: the filtering approach. *J. Fluid Mech.* **238** (1992), 325–336.

[63] E. Jeong and S. S. Girimaji. Partially-Averaged Navier-Stokes Method for Turbulence Simulations - Flow Past a Square Cylinder. *J. Fluid. Eng.-T ASME* **132** (2010), pages.

[64] S. Lakshmipathy and S. S. Girimaji. Partially-Averaged Navier-Stokes Method for Turbulence Simulations - Flow Past a Circular Cylinder. *J. Fluid. Eng.-T ASME* **73** (2010), pages.

[65] S. Lakshmipathy and S. S. Girimaji. Partially-Averaged Navier-Stokes Method for Turbulent Flows - $k-\omega$ implementation. (2006), pages.

[66] J. Ma, S. Peng, L. Davidson, and F. Wang. A Low Reynolds Number Variant of Partially-Averaged Navier-Stokes Model for Turbulence. *Int. J. Heat Fluid Fl.* **2011** (2011), 652–669.

[67] P. A. Durbin. Near-Wall Turbulence Closure Modeling Without Damping Functions. *Theor. Comp. Fluid Dyn.* **3** (1991), 1–13.

[68] K. Hanjalić, M. Popovac, and Hadžiabdić. A robust near-wall elliptic-relaxation eddy-viscosity turbulence model for CFD. *Int. J. Heat Fluid Fl.* **25** (2004), 1047–1051.

[69] B. Basara, S. Krajnović, and S. S. Girimaji. PANS methodology applied to elliptic relaxation-based eddy viscosity transport model. *Proceedings of Turbulence and Interactions* (2009), pages.

[70] B. Basara, S. Krajnović, S. S. Girimaji, and Z. Pavlovic. Partially Averaged Navier-Stokes Method for Turbulence Simulations: Near-Wall Eddy Viscosity Transport Model Implementation. *AIAA Journal* **49 (12)** (2011), 2627–2636.

[71] S. Krajnović. Flow around a tall finite cylinder explored by large eddy simulation. *J. Fluid Mech.* **676** (2011), 294–317.

[72] S. Krajnović, R. Lárusson, and B. Basara. Superiority of PANS compared to LES in predicting a rudimentary landing gear flow with affordable meshes. *Int. J. Heat Fluid Fl.* **37** (2012), 109–122.

[73] Proceedings (CDROM) of the AIAA-NASA workshop on benchmark problems for airframe noise computations-I (BANC-I) (June 9-11, 2010).

[74] P. R. Spalart and K. M. Mejia. Analysis of Experimental and Numerical Studies of the Rudimentary Landing Gear (2011), pages.

[75] A. Frendi, A. Tosh, and S. S. Girimaji. Flow past a backward-facing step: Comparison of PANS, DES and URANS results with experiments. *Int. J. Comput. Methods Eng. Sci Mech.* **8** (2007), 23–38.

[76] S. S. Girimaji and K. S. Abdol-Hamid. "Partially-Averaged Navier-Stokes for Turbulence: Implementation and Validation". *43rd AIAA Aerospace Science Meeting and Exhibit*. Reno, Nevada, AIAA-paper 2005-0502, 2005.

[77] B. Basara, S. Krajnović, and S. S. Girimaji. "PANS VS. LES for computations of the flow around a 3D bluff body". *7th International ERCOFTAC Symposium on "Engineering Turbulence Modelling and Measurements*. Limassol, Cyprus., 2008.

[78] AVL Fire CFD Solver. *FIRE CFD Solver Users Guide* **v2013** (2013).

[79] P. Holmes, J. L. Lumley, G. Berkooz, and C. W. Rowley. *Turbulence, Coherent Structures, Dynamical Systems and Symmetry*. 2nd paperback. Cambridge: Cambridge University Press, 2012.

[80] C. W. Rowley, I. Mezić, S. Bagheri, P. Schlatter, and D. Henningson. Spectral analysis of nonlinear flows. *J. Fluid Mech.* **645** (2009), 115–127.

[81] P. J. Schmid. Dynamic mode decomposition for numerical and experimental data. *J. Fluid Mech.* **656** (2010), 5–28.

[82] L. Cordier and M. Bergmann. "Proper Orthogonal Decomposition: An Overview". *Post-Processing of Experimental and Numerical Data*. Ed. by P. Millan and M. Riethmuller. VKI Lecture Series 2003-03. Von Kármán Institut for Fluid Dynamics, 2003.

[83] L. Cordier, J. Delville, and J.-P. Bonnet. "Review of Some Fundamentals of Data Processing: Proper Orthogonal Decomposition". *Handbook of Experimental Fluid Mechanics*. Springer-Verlag, 2007.

[84] A. E. Deane, I. G. Kevrekidis, G. E. Karniadakis, and S. A. Orszag. Low-dimensional models for complex geometry flows: Application to grooved channels and circular cylinders. *Phys. Fluids A* **3** (1991), 2337–2354.

[85] B. R. Noack, K. Afanasiev, M. Morzyński, G. Tadmor, and F. Thiele. A hierarchy of low-dimensional models for the transient and post-transient cylinder wake. *J. Fluid Mech.* **497** (2003), 335–363.

[86] J. Delville, L. Ukeiley, L. Cordier, J. Bonnet, and M. Glauser. Examination of large-scale structures in a turbulent plane mixing layer. Part 1. Proper orthogonal decomposition. *J. Fluid Mech.* **391** (1999), 91–122.

[87] M. Rajaee, S. Karlsson, and L. Sirovich. Low-dimensional description of free-shear-flow coherent structures and their dyanmical behaviour. *J. Fluid Mech.* **258** (1994), 1–29.

[88] L. Ukeiley, L. Cordier, R. Manceau, J. Delville, J. P. Bonnet, and M. Glauser. Examination of large-scale structures in a turbulent plane mixing layer. Part 2. Dynamical systems model. *J. Fluid Mech.* **441** (2001), 61–108.

[89] W. Cazemier, R.W.C.P. Verstappen, and A.E.P. Veldman. Proper orthogonal decomposition and low-dimensional models for driven cavity flows. *Phys. Fluids* **10** (1998), 1685–1699.

[90] N. Aubry, P. Holmes, J. L. Lumley, and E. Stone. The Dynamics of coherent structures in the Wall Region of a Turbulent Boundary Layer. *J. Fluid Mech.* **192** (1988), 115–173.

[91] D. Rempfer. "Kohärente Strukturen und Chaos beim laminar-turbulenten Grenzschichtumschlag (transl.: Coherent structures and chaos of the laminar-turbulent boundary-layer transition)". (Part of this work has been published by Rempfer, D. and Fazle, F.H. (1994) in J. Fluid Mech. **260** & **275**). PhD thesis. Fakultät Verfahrenstechnik der Universität Stuttgart, 1991.

[92] D. Rempfer and F. Fasel. Evolution of three-dimensional coherent structures in a flat-plate boundary-layer. *J. Fluid Mech.* **260** (1994), 351–375.

[93] D. Rempfer and F. H. Fasel. Dynamics of three-dimensional coherent structures in a flat-plate boundary-layer. *J. Fluid Mech.* **275** (1994), 257–283.

[94] G. Galletti, C. H. Bruneau, L. Zannetti, and A. Iollo. Low-order modelling of laminar flow regimes past a confined square cylinder. *J. Fluid Mech.* **503** (2004), 161–170.

[95] B. R. Noack, M. Morzyński, and G. (Tadmor. *Reduced-Order Modelling for Flow Control*. CISM Courses and Lectures 528. Berlin: Springer-Verlag, 2011.

[96] B. R. Noack, M. Schlegel, B. Ahlborn, G. Mutschke, M. Morzyński, P. Comte, and G. Tadmor. A finite-time thermodynamics of unsteady fluid flows. *J. Non-Equilibr. Thermodyn.* **33** (2008), 103–148.

[97] Z. Wang, I. Akhtar, J. Borggaard, and T. Iliescu. Two-level discretizations of nonlinear closure models for proper orthogonal decomposition. *J. Comp. Phys.* **230** (2011), 126–146.

[98] Z. Wang, I. Akhtar, J. Borggaard, and T. Iliescu. Proper orthogonal decomposition closure models for turbulent flows: A numerical comparison. *Comput. Methods Appl. Mech. Engrg.* **237–240** (2012), 10–26.

[99] L. Sirovich. Turbulence and the dynamics of coherent structures, Part I: Coherent structures. *Quart. Appl. Math.* **XLV** (1987), 561–571.

[100] X. Ma and G. E. Karniadakis. A low-dimensional model for simulating three-dimensional cylinder flow. *J. Fluid Mech.* **458** (2002), 181–190.

[101] B. R. Noack, P. Papas, and P. A. Monkewitz. The need for a pressure-term representation in empirical Galerkin models of incompressible shear flows. *J. Fluid Mech.* **523** (2005), 339–365.

[102] L. Cordier, B. R. Noack, G. Tissot, G. Lehnasch, J. Delville, M. Balajewicz, G. Daviller, and R. K. Niven. Identification strategies for model-based control. *Exp. Fluids* **54** (2013), 1–21.

[103] E. Kaiser, B. Noack, L. Cordier, A. Spohn, M. Segond, M. Abel, G. Daviller, J. Östh, S. Krajnović, and R. T. Niven. Cluster-based reduced-order modelling of a mixing layer. *Revised manuscript submitted to the Journal of Fluid Mechanics* (2014).

[104] Y. Sakuma and A. Ido. Wind Tunnel Experiments on Reducing Separated Flow Region Around Front Ends of Vehicles on Meter-Gauge Railway Lines. *Quarterly Report of RTRI* **50**.1 (2009), 20–25.

[105] F. Alam and S. Watkins. "Lateral stability of a double stacked container wagon under crosswinds". *Proceedings of the International Conference on Mechanical Engineering 2007 (ICME2007)*. Dhaka, Bangladesh, 2007, pp. 225–242.

[106] M. Grandemange, M. Gohlke, and O. Cadot. Turbulent wake past a three-dimensional blunt body. Part 1. global modes and bi-stability. *J. Fluid Mech.* **722** (2013), 51–84.

[107] S. Ahmed, G. Ramm, and G. Faltin. Some salient features of the time averaged ground vehicle wake. *Society of Automotive Engineers, SAE Inc* **840300** (1984).

[108] E. Duell and A. George. Experimental study of a ground vehicle body unsteady near wake. *Society of Automotive Engineers, SAE Inc* **1999-01-0812** (1999).

[109] H. Lienhart and S. Becker. Flow and turbulent structure in the wake of a simplified car model. *Society of Automotive Engineers, SAE Inc* **2003-01-0656** (1984).

[110] J.-F. Beaudoin and J.-L. Aider. Drag and lift reduction of a 3d bluff body using flaps. *Exp. Fluids* **44** (2013), 491–501.

[111] S. Krajnović. "LES investigation of passive flow control around an ahmed body". *International Mechanical Engineering Congress & Exposition*. Vol. 1. Paper IMECE2013-62373. San Diego, CA, USA: ASME, 2013, pp. 305–315.

[112] J.-L. Aider, J.-F. Beaudoin, and J. E. Wesfreid. Drag and lift reduction of a 3D bluff-body using active vortex generators. *Exp. Fluids* **48** (2010), 771–789.

[113] A. Brunn, W. Nitsche, L. Henning, and R. King. Application of slope-seeking to a generic car model for active drag control. *IAA Paper 2008-6734*. (2008).

[114] S. Krajnović and J. Fernandes. Numerical simulation of the flow around a simplified vehicle model with active flow control. *Int. J. Heat Fluid Fl.* **32** (2011), 192–200.

[115] M. Pastoor, L. Henning, B. R. Noack, R. King, and G. Tadmor. Feedback shear layer control for bluff body drag reduction. *J. Fluid Mech.* **608** (2008), 161–196.

[116] S. Krajnović and L. Davidson. Numerical Study of the Flow Around the Bus-Shaped Body. *J. Fluid. Eng.-T ASME* **125** (2003), 500–509.

[117] B. Khalighi, K.-H. Chen, and G. Laccarino. Unsteady aerodynamic flow investigation around a simplified square-back road vehicle with drag reduction devices. *J. Fluid. Eng.-T ASME* **134** (2012), pages.

[118] R. Verzicco, M. Fatica, G. Laccarino, and P. Moin. Large Eddy Simulation of a road vehicle with drag-reduction devices. *AIAA J.* **40** (2002), 2447–2455.

[119] A. Grandemange, M. Gohlke, and O. Cadot. Bi-stability in the turbulent wake part parallelepiped bodies with various aspect ratios and wall effects. *Phys. Fluids* **25** (2013), 095103.

[120] A. Grandemange, M. Gohlke, and O. Cadot. Reflectional symmetry breaking of the separated flow over three-dimensional bluff bodies. *Phys. Rev. E* **86** (2012), 035302.

[121] L. D. Landau and E. M. Lifshitz. *Fluid Mechanics*. 2nd engl. Course of Theoretical Physics Vol. 6. Oxford: Pergamon Press, 1987.

[122] S. Muzaferija and D. Gosman. Finite-Volume CFD Procedure and Apaptive Error Control Strategy for Grids of Arbitrary Topology. *J. Comp. Phys.* **138** (1996), 766–787.

[123] B. R. Noack, M. Schlegel, M. Morzyński, and G. Tadmor. System reduction strategy for Galerkin models of fluid flows. *Int. J. Numer. Meth. Fluids* **63**.2 (2010), 231–248.

[124] J. Östh, B. R. Noack, and Krajnović. A new drag equation for POD models. *In preparation for the J. Fluid Mech.* (2014).

[125] J. Östh, S. Krajnović, D. Barros, L. Cordier, B. Noack, J. Borée, and T. Ruiz. "Active flow control for drag reduction of vehicles using large eddy simulation, experimental investigations and reduced order modelling". *Proceedings of the* 8th International Symposium On Turbulent and Shear Flow Phenomena (TSFP-8). Poitiers, France, 2013.

[126] J. Östh and S. Krajnović. "Large Eddy Simulation of the Flow around one Single-Stacked Container Freight Wagon". *Proceedings of the First International Conference on Railway Technology: Research, Development and Maintenance*. Ed. by J. Pombo. Vol. 1145. Lecture Notes in Computer Science. Civil-Comp Press, Stirlingshire, Scotland, paper 162, 2012, pp. 51–66.

[127] J. Östh and S. Krajnović. "A LES Study of a Simplified Tractor-Trailer Model". *The Aerodynamics of Heavy Vehicles III: Trucks, Buses, and Trains*. Vol. 1. Potsdam, Germany, 2010.

[128] M. Schlegel, B. R. Noack, P. Comte, D. Kolomenskiy, K. Schneider, M. Farge, J. Scouten, D. M. Luchtenburg, and G. Tadmor. "Reduced-order modelling of turbulent jets for noise control". *Numerical Simulation of Turbulent Flows and Noise Generation: Results of the DFG/CNRS Researcg Groups FOR 507 and FOR 508*. Notes on Numerical Fluid Mechanics and Multidisciplinary Design (NNFM). Springer-Verlag, 2009, pp. 3–27.

[129] Z. J. Wang. Improved formulation for geometric properties of arbitrary polyhedra. *AIAA Journal* **37** (1999), 1326–1327.

Appendix A. Details of the solver

Solver

This appendix describes the theory and numerical discretization of the incompressible Navier-Stokes equations, and outlines the solution algorithm that has been used in this thesis.

Computational grid

A a general hexahedral cell as depicted in figure 6.1a) is considered. The cell has 8 vertices, $\{\nu_1, ..., \nu_8\}$, and 6 faces in total. The primary entities defining the computational grid in the initial state are the vertices and the faces. The location of the vertices is stored in a matrix $X_v \in R^{N_v} \times R^3$. Thus, $X_v(k,1)$, $X_v(k,2)$ and $X_v(k,3)$, correspond to the x, y and z coordinates of the k-th vertex, and N_v is the total number of vertices in the grid. The faces are defined by a matrix $f \in R^{N_f} \times R^6$. The first 4 entries of each row in the matrix f correspond to the global indices of the vertices defining the face, and the two last entries specifies the cell ownership of the face and the neighbouring cell. A general face j, b and the neighbouring cells, P and R, is shown in Fig. 6.1b). Denotation of the face as either j or b is to differentiate between interior faces of the grid and faces on the boundary. An interior face j is defined by 4 vertices $\{v_1, v_2, v_3, v_4\}$. The j-th row in f is: $f(j,:) = [v_1, v_2, v_3, v_4, P, R]$. P is the index to the cell located to the "left" of the face, and R is the index of the cell located to the "right" of the face. The area vector $\vec{A}_j$ of face j is oriented such that it always points from cell P to cell R. The area of the face j is given by $A_j = |\vec{A}_j|$ and the outward unit normal vector of face j is given by the normalized area vector, $\vec{n}_j = \vec{A}_j / A_j$. For a boundary face, b, the row b of f is given by $f(b,:) = [v_1, v_2, v_3.v_4, P, 0]$. Boundary faces are thus indicated by having a zero at position 6. Thus, boundaries will always be located to the "right" of all faces. The two primary entities, vertices and faces, together with a list of faces belonging to the different boundary zones (face zones) and the corresponding boundary condition, define the computational domain completely. From these entities other quantities such as the area vectors, directional vectors, interpolation factors and cell volumes are computed. The directional vector of each face, $\vec{d}_j$, is the vector between cell R and cell-center of cell P, $\vec{d}_j = \vec{r}_R - \vec{r}_P$, for interior faces, and the vector between the face-center and the cell-center of cell P for boundary faces ($\vec{d}_j = \vec{r}_R - \vec{r}_j$). The face center coordinates is calculated by a split of the face into two triangles as in Fig. 6.1c), $t_1 = \{v_1\ v_2\ v_3\}$ and $t_2 = \{v_1\ v_3\ v_4\}$.

The centerpoint of each triangle is calculated as the average position of the three vertices defining the triangle, and the center of the face is given by the averaged value of the centers of the two triangles, thus: $\vec{r}_{t_1} = (\vec{r}_{v_1} + \vec{r}_{v_3} + \vec{r}_{v_4})/3$ and $\vec{r}_{t_2} = (\vec{r}_{v_1} + \vec{r}_{v_2} + \vec{r}_{v_3})/3$ and $\vec{r}_f = (\vec{r}_{t_1} + \vec{r}_{t_2})/2$. This splitting procedure of each face to triangular parts is done since the center point of a quadrangle is not the same as the average position of the four vertices for non-orthogonal quadrangles. The face center coordinates, $\vec{r}_f$, are stored in a matrix $X_f \in R^{N_f} \times R^3$ where $X_f(j,1)$, $X_f(j,2)$ and $X_f(j,3)$, correspond to the x, y and z coordinates of the face center of the j-th face, respectively. The area vector of a face, $\vec{A}$,

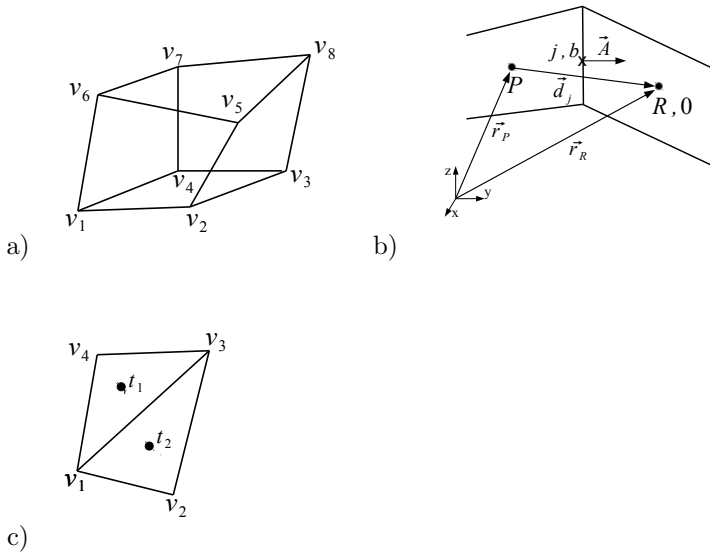

Figure 6.1: a) a general hexahedral computational cell with 8 vertices. b) a general face j (interior face) or b (boundary face). c) Schematic depiction of the split of each quadrangular face into two triangular parts in order to compute area vectors.

is calculated by taking the sum of the two area vectors of the triangles t_1 and t_2. The area vectors of the triangle t_1 is given by the cross-product $\vec{A}_{t_1} = \frac{1}{2}(\vec{r}_{v_2} - \vec{r}_{v_1}) \otimes (\vec{r}_{v_3} - \vec{r}_{v_1})$ and the area vector of the triangle t_2 is $\vec{A}_{t_2} = \frac{1}{2}(\vec{r}_{v_4} - \vec{r}_{v_1}) \otimes (\vec{r}_{v_3} - \vec{r}_{v_1})$. Thus, $\vec{A} = (\vec{A}_{t_1} + \vec{A}_{t_2})$. The area vectors of each face are stored in a matrix $A \in R^{N_f} \times R^3$. The volume of each computational cell, V_P, is computed using the following expression:

$$V_P = \frac{1}{3} \sum_{j=1}^{n_{f,P}} \vec{r}_j \cdot \vec{A}_j. \tag{6.1}$$

In (6.1), $n_{f,P}$ refers to the number of faces belonging to cell P. In the current version of the code, hexahedral cells are assumed, thus $n_{f,P} = 6$ for all cells. In general, the volume of a closed domain is given by the volume integral over the domain, $V = \int_V dV$. The divergence of the position vector is equal to one. Thus, $V = \int_V \nabla \cdot \vec{r} dV = \int_A \vec{r} \cdot d\vec{S}$. The cell-center, $\vec{r}_P$, of a cell P, is found by the following expression [129], obtained in a similar manner as (6.1):

$$\vec{r}_P = \frac{3}{4} \left[\sum_{j=1}^{n_{f,P}} (\vec{r}_j \cdot \vec{A}_j) \vec{r}_j \right] / \left[\sum_{j=1}^{n_{f,P}} (\vec{r}_j \cdot \vec{A}_j) \right] \tag{6.2}$$

The locations of the cell centers are stored in a matrix $X_c \in R^{N_c} \times R^3$, where N_c is the total number of control volumes (cells) in the grid. It should be noted that all of the above

calculations can very easily be generalized to be valid for an arbitrary computational cell (defined by having abitrary number of faces) in the code since the only difference between hexahedrals ($n_f = 6$), prisms ($n_f = 5$), and tetrahedrals ($n_f = 4$) is the number of faces, n_f, of the cell.

Discretization

The incompressible Navier-Stokes equations in conservative form are:

$$\nabla \cdot \vec{V} = 0, \tag{6.3}$$

$$\frac{\partial \rho\phi}{\partial t} + \nabla \cdot (\rho\phi\vec{V}) - \nabla \cdot (\Gamma \nabla\phi) = S_\phi. \tag{6.4}$$

Here, $\vec{V} = (u, v, w)$, is the velocity field vector, ϕ is a generic variable which can be either u,v, or w. ρ is the density of the working fluid and Γ is the effective viscosity of the fluid (containing both physical viscosity and turbulent viscosity due to the specific turbulence model applied). The pressure gradient ,∇p, has been included in the general source term S_ϕ. By integrating (6.4) over a computational cell, P, and expressing the integrals as surface integrals by making use of Gauss theorem, we obtain:

$$\frac{\partial}{\partial t}\left(\int_{V_P} \rho\phi dV\right) + \int_{A_p} \rho\phi\vec{V} \cdot d\vec{A} - \int_{A_p} \Gamma(\nabla\phi) \cdot d\vec{A} = \int_{V_P} S_\phi dV. \tag{6.5}$$

In the next step, the integrals are approximated by the mid-point rule, $\int_A (...)d\vec{A} \approx (...)\vec{A}$ and $\int_V (...)dV \approx (...)V_p$, and expressed as a sum over all of the faces of cell P:

$$\frac{\partial}{\partial t}(\rho\phi V_p) + \sum_{j=1}^{n_f} (\rho\vec{V} \cdot \vec{A})_j \phi_j - \sum_{j=1}^{n_f} (\Gamma(\nabla\phi) \cdot \vec{A})_j = S_\phi^P \cdot V_P, \qquad P = 1, ..., N_c. \tag{6.6}$$

From here, the sums are dropped for convenience and implied implicitly. The first term is the temporal term, the second term is the convective flux, the third term is the diffusive flux, and the last term is a source term containing the pressure gradient, which is treated explicitly (i.e. values from the previous iteration are used when computing the term.) The pressure gradient is computed in a similar manner as the volume, V_P, of a cell (see (6.1)). $\rho(\vec{V} \cdot \vec{A})_j = \dot{m}_j$ is the mass-flow through face j. This is calculated explicitly using the velocity values of the previous iteration. ϕ_j is the quantity of ϕ at face j. The diffusive term becomes [78]:

$$\overline{\Gamma}_j \frac{A_j^2}{\vec{A} \cdot \vec{d}_j}(\phi_R - \phi_P) + \overline{\Gamma}_j \overline{\nabla\phi}_j \cdot \left(\vec{A}_j - \frac{A_j^2}{\vec{A}_j \cdot \vec{d}_j}\vec{d}_j\right) \tag{6.7}$$

Here, $\overline{\phi}$ denotes linear interpolation. Defining the interpolation factor as $f_j = |\vec{r}_R - \vec{r}_j|/(|\vec{r}_j - \vec{r}_P| + |\vec{r}_R - \vec{r}_j|)$, and variable ϕ at a face j is found by linear interpolation from the neighbouring cells as $\overline{\phi}_j = f_j\phi_P + (1 - f_j)\phi_R$. The second term in (6.7) arises due to non-orthogonality between cell P and cell R. The expression in (6.7) can be derived by drawing a computational cell around the center of face j, having vertices in the centers of the cells P and R, and the vertices defining the face j. With $D_j = \overline{\Gamma}_j A_j^2/(\vec{A} \cdot \vec{d}_j)$, adding the second term in (6.7) to the general source term S_ϕ^P and dropping the temporal term for the moment, (6.7) is now written as:

$$\dot{m}_j\phi_j = D_j(\phi_R - \phi_P) + S_\phi^P \cdot V_P. \tag{6.8}$$

The last step is to decide the numerical scheme of the convective term. Here, the blending scheme between the First Order Upwind scheme and the Central Differencing Scheme is described, as this is the scheme that has been used in this thesis. Firstly, the upwind scheme is described:

$$\phi_j^{UDS} = \phi_P g^{UDS} + \phi_R(1 - g^{UDS}) \tag{6.9}$$

Where the function g^{UDS} is defined as

$$g^{UDS} = \begin{cases} 0 & \text{if } \dot{m}_j < 0; \\ 1 & \text{if } \dot{m}_j \geq 0. \end{cases} \tag{6.10}$$

In order to formulate the blending scheme, a "flow-oriented" interpolation factor is introduced:

$$f_j^* = \begin{cases} 1 - f_j & \text{if } \dot{m}_j \geq 0; \\ f_j & \text{if } \dot{m}_j < 0. \end{cases} \tag{6.11}$$

The blending scheme then takes the following form:

$$\phi_j = \phi_j^{UDS} + \gamma_\phi f_j^* \frac{\dot{m}_j}{|\dot{m}_j|}(\phi_R - \phi_P). \tag{6.12}$$

Where $\gamma_\phi \in [0, 1]$ is the blending factor. $\gamma_\phi = 0$ yields a pure first order upwind scheme, and $\gamma_\phi = 1$ yields a pure Central Differencing Scheme.

Equation (6.8) can now be written for a cell P as:

$$a_P\phi_P = \sum_{R=1}^{n_P} a_R\phi_R + S_\phi, \tag{6.13}$$

Linear system

Equation (6.13) is a system of linear equations of the form $A\phi = S$. Since $\phi = u, v, w$, we have three coupled linear equations systems:

$$Au = S_u \tag{6.14}$$
$$Av = S_v \tag{6.15}$$
$$Aw = S_w \tag{6.16}$$

These three equations are the discretized momentum equations. Implicit underrelaxation is applied in order to iteratively solve the equations:

$$\phi^k = \phi^{k-1} + \alpha_\phi(\phi^{new} - \phi^{k-1}), \tag{6.17}$$

where $0 < \alpha_\phi \leq 1$ is the underrelaxation factor. Inserting (6.17) in (6.13) gives the modified linear system:

$$a_P^* \phi_P = \sum_{R=1}^{n_P} a_R \phi_R + S_\phi^*, \tag{6.18}$$

where the modified a_P^* and S_ϕ^* are:

$$a_P^* = \frac{a_P}{\alpha_\phi} \ , \ S_\phi^* = \frac{1-\alpha_\phi}{\alpha_\phi} a_P \phi^{k-1} \tag{6.19}$$

Equation 6.18 is the linear system that is actually solved in the code.

Calculation of mass flow

In order to calculate the mass flow, $\dot{m}_j = \rho \vec{V}_j \cdot \vec{A}_j$, at each face j, the velocity vector, $\vec{V}_j$, needs to be known at the face. This is obtained by Rhie-Chow interpolation [122, 78]:

$$\vec{V}_j = \overline{\vec{V}}_j - \frac{1}{2}\left(\frac{V_p}{a_p} + \frac{V_R}{a_R}\right) \frac{\vec{A}_j}{\vec{A}_j \cdot \vec{d}_j} \left[(P_R - P_P) - \overline{\nabla p}_j \cdot \vec{d}_j\right] \tag{6.20}$$

Pressure correction

The mass flow obtained by using (6.20) is called $\dot{m}_j^*$. This mass flow do not satisfy the continuity equation in general, but results in a mass source for each cell:

$$S_m^* = \sum_{j=1}^{n_f} \dot{m}_j^*. \tag{6.21}$$

This mass source must be driven to zero. This is done by a correction of the velocities and the pressure:

$$\vec{V}_P = \vec{V}_P^* + \vec{V}_P^{'} \;\; ; \;\; P_P = P_P^* + P_P^{'} \tag{6.22}$$

This leads to a linear system where the unknowns are the pressure corrections $P_P^{'}$ [78]:

$$a_P^{'} P_P^{'} = \sum_{j=1}^{n_f} a_{R_j}^{'} P_{R_j}^{'} - S_m^* \tag{6.23}$$

Update variables

After obtaining the pressure corrections, the pressure field and the velocities need to be updated before proceeding to the next iteration. This is done in the following way [78]:

$$\vec{V}_P = \vec{V}_P^* - \frac{V_P}{a_P}(\nabla P_P^{'}) \tag{6.24}$$

$$P_P = P^* + \alpha_P P_P^{'} \tag{6.25}$$

$$\dot{m}_j = \dot{m}_j^* + (a_{R_j} P_{R_j} - a_{R_j} P_P) \tag{6.26}$$

Calculation of residuals

The residuals are calculated the following way [78]:

$$\sum_{i=1}^{N_c} |a_P^* \phi_p - \sum_{j=1}^{n_i} a_R \phi_R - S_\phi^*| / \sum_{i=1}^{N_c} |a_P^* \phi_p| \tag{6.27}$$

Time-integration

The temporal term was dropped in (6.8) for convenience when outlining the solution details in the subsections above, as this term stand alone and do not influence the other terms directly. Here, the term is re-introduced and the time-integration scheme is outlined. The semi-discretized equation in (6.7) takes the general form of a first order differential equation:

$$\frac{d\psi}{dt} + \Phi(\phi, t) = 0 \quad , \quad \psi = (\rho V \phi)_P. \tag{6.28}$$

Here, the convective and diffusive fluxes and the source terms have ben replaced by Φ. Numerous time-integration of various order of errors exist. In this work, a three time level scheme has been used which is second order accurate. The scheme takes the following time-discrete form:

$$\left(\frac{d\psi}{dt}\right)_n = \frac{3\psi^n - 4\psi^{n-1} + \psi^{n-2}}{2\Delta t_n} = -\Phi^n. \tag{6.29}$$

Here, t_n denote the discrete time step size at time t_n, and ^{n}, $^{n-1}$ and $^{n-2}$ denote quantity at the time t_n, t_{n-1} and t_{n-2}, respectively.

Solution algorithm

The solution algorithm is as follows:

1. Initialize solution, $\vec{V}^0 = 0$ and $P^0 = 0$
2. Solve (6.18) for $\phi = u$, $\phi = v$ and $\phi = w$ to obtain $\vec{V}^*$
3. Calculate mass flow, $\dot{m}_j^*$, by (6.20) using $\vec{V}^*$.
4. Solve for the pressure correction using (6.23)
5. Update the variables using equations (6.24)-(6.26), and obtain $\vec{V}^1$ and P^1
6. Repeat 2 - 6 until convergence within the time step
7. March the solution forward in time
8. Repeat 1 - 7 until a sufficiently long time domain has been simulated

One iteration of the steps 2 - 5 is refered to as an “outer iteration”.